

A comprehensive study of δ Scuti-type pulsators in eclipsing binaries: oscillating eclipsing Algols

T. B. Pawar,^{1,2,*}, A. Miszuda,³, K. G. Hełminiak,¹, F. Marcadon,³, A. Moharana,^{1,4}, G. Pawar,¹, and M. Konacki¹

¹ Nicolaus Copernicus Astronomical Center, Polish Academy of Sciences, ul. Rabiańska 8, 87-100 Toruń, Poland

² Villanova University, Dept. of Astrophysics and Planetary Sciences, 800 East Lancaster Avenue, Villanova, PA 19085, USA

³ Nicolaus Copernicus Astronomical Center, Polish Academy of Sciences, ul. Bartycka 18, 00-716 Warszawa, Poland

⁴ Astrophysics Group, Keele University, Staffordshire, ST5 5BG, U.K.

ABSTRACT

Eclipsing double-lined spectroscopic binaries (SB2s) hosting δ Scuti-type pulsators offer a unique laboratory for simultaneously constraining stellar geometry and interior structure. In this study, we present a comprehensive analysis of five oscillating eclipsing Algol (oEA) binaries. By combining high-precision, short-cadence TESS photometry with multi-epoch high-resolution spectroscopy, we derive precise stellar and orbital parameters. Frequency power spectra were obtained using residuals from binary modelling. We further investigate the evolutionary history of these systems using a grid of MESA binary evolution simulations. Our analysis suggests that the systems must have undergone either case A or case B mass transfer, with the primary components repositioned in the Hertzsprung–Russell diagram and now pulsating in the δ Scuti regime, while the cooler secondaries are underluminous and inflated, filling their Roche lobes. This study contributes to the growing catalog of well-characterised oEA systems and our understanding of the effects of mass-transfer on the fate of these short-period binaries.

Key words. binaries: eclipsing – stars: oscillations – variables: delta Scuti – asteroseismology – stars: individual (HD 139774, SW Pup, HD 202042, GP Cet, TZ Eri)

1. Introduction

Eclipsing binaries (EBs) that are also double-lined spectroscopic binaries (SB2s) are among the most important tools for determining absolute stellar parameters. Their light curves (LCs) provide insights into their geometric configurations, particularly stellar radii relative to the orbital separation. Stellar inclinations are best constrained in EBs (Murphy et al. 2018). However, LCs alone do not provide information about stellar masses, which are crucial for understanding stellar evolution.

Determining stellar masses requires radial velocity (RV) measurements across the full orbital phase; hence, spectroscopic follow-up is essential to obtain the absolute parameters necessary for understanding stellar structure and evolution. This task becomes particularly challenging for systems with longer orbital periods, as phase coverage of the binary’s orbit requires longer time baselines and is more difficult for observations planning and scheduling (Torres et al. 2010).

EBs provide highly accurate and precise mass and radius measurements, making them crucial for testing stellar evolution models. However, these fundamental parameters alone do not reveal much about a star’s internal structure, energy transport mechanisms, or chemical composition.

Stellar oscillations are driven by intrinsic mechanism that produce observable changes in star’s brightness. Careful investigation of these brightness variation can thus inform us about the physics of the driving mechanism. One of the classical pulsators, known as δ Scuti-type stars. Their masses typically range from 1.5–2.0 M_{\odot} . Recent studies have found that many δ Scuti-type stars are members of EBs (Liakos & Niarchos 2017a,b; Kahra-

man Aliçavuş et al. 2017, 2022a; Chen et al. 2022; Kahraman Aliçavuş et al. 2023). These systems offer an excellent opportunity to obtain precise geometrical configurations. Moreover, they allow us to probe stellar interiors through a detailed asteroseismic analysis of the pulsating component (Liakos & Niarchos 2020; Miszuda et al. 2022).

One of the main hindrance in such studies was the quality of data from the ground based telescopes. In order to study the complex pulsation spectra, a long baseline photometric dataset is required. Continuous, high-precision photometric data from space missions – first from *Kepler* (Koch et al. 2010) with its four-year baseline and now from the short-cadence observations provided by the Transiting Exoplanet Survey Satellite (TESS; Ricker et al. 2015) – have greatly enhanced our ability to detect and analyse candidate pulsators in EBs.

The remarkable success of the *Kepler* and TESS space missions has led to the detection of over 1,000 δ Scuti-type pulsators in EBs. However, determining the absolute parameters of these systems remains challenging, and thus, only a small subset (~10%) has been characterised with high precision so far (Liakos 2024). Several catalogs (Liakos & Niarchos 2017; Kahraman Aliçavuş et al. 2017; Antoci et al. 2019; Chen et al. 2022; Kahraman Aliçavuş et al. 2022b) and studies (e.g., Murphy et al. 2018) have investigated the statistical properties of these systems, revealing empirical relationships between their physical, orbital, and pulsational characteristics.

A subset of these binaries falls into the short-period, semi-detached category with extreme mass ratios, indicating a history of mass transfer. This process alters stellar lifetimes, temperatures, and luminosities, shifting their positions on the Hertzsprung–Russell diagram. Depending on whether donor is on the main sequence, post-main sequence, or Asymptotic Gi-

* E-mail: pawartilak7@gmail.com

ant Branch (AGB) phase, mass transfer is classified as Case A, Case B, or Case C, respectively (Kippenhahn & Weigert 1967; Paczyński 1971; Eggleton 2006). In Case A, the donor loses mass while still burning hydrogen in its core, evolving into a helium white dwarf or a hot subdwarf, depending on factors like the core mass, efficiency of mass transfer and the mass ratio between the donor and accretor (Han et al. 2002, 2003). In Case B, the donor has exhausted core hydrogen, and if mass loss occurs before helium ignition, it becomes either a helium white dwarf or a helium-burning star, later evolving into a carbon-oxygen white dwarf. The accretor, in both cases, gains mass, often moving toward the subgiant or giant phase earlier than in single-star evolution. Case C mass transfer occurs when the donor star fills its Roche lobe after exhausting helium in its core. This often leads to dynamically unstable mass transfer.

Systems such as those in our sample represent semi-detached Algol-type EBs with pulsating components. These pulsators have experienced significant interaction and, as a result, differ from the typical δ Scuti stars found in detached EBs (Mkrtichian et al. 2002). Mkrtichian et al. (2004) introduced the term “oEA” (oscillating eclipsing Algol) to describe these systems. These binaries serve as excellent astrophysical laboratories for studying binary evolution on shorter timescales, examining the effects of mass transfer on pulsations, and comparing the impact of accretion on stellar evolution against traditional single-star models (Mkrtichian et al. 2002).

One of the primary challenges in fully characterizing these systems is the availability of high-quality RV measurements, which are essential for deriving precise stellar masses. This issue has become even more pronounced with the advent of large-scale photometric surveys that provide extensive LC data, yet remain insufficient for determining absolute parameters without complementary RV data. Without these crucial measurements, our understanding of these systems remains incomplete – like a bottle of finely aged wine, enticingly within reach, yet sealed by the unyielding cork of missing RV observations. In most cases, absolute masses cannot be determined without RVs, leaving many systems with unresolved characteristics.

The Comprehensive Research with Échelles on the Most Interesting Eclipsing Binaries project (CRÉME; Helminiak et al. 2012, 2015, 2021; Ratajczak et al. 2013) was initiated to address this gap in RV data. The survey systematically monitored a sample of more than 350 EBs, obtaining multi-epoch spectra to refine our understanding of their fundamental properties.

In this paper, we present a detailed analysis of five oEA systems identified within the CRÉME sample. Sections 2 and 3 outline the data collection and curation process, followed by an in-depth discussion of RV and LC modeling. Using the derived system parameters, we perform frequency analysis on the residuals of the binary model fit and conduct an evolutionary analysis. Finally, we discuss our results and present our conclusions.

2. Target Selection and Observations

To identify potential δ Scuti-type pulsators, systems were pre-selected based on their projected minimum masses, ensuring they fell within the expected mass range for these pulsators. Among these, five systems with exceptionally low mass ratios stood out as strong oEA candidates: TIC 64437380 (HD 139774), TIC 82474821 (SW Pup), TIC 126945917 (HD 202042), TIC 10756751 (GP Cet), and TIC 37817410 (TZ Eri). These systems provide valuable opportunities to study the ef-

fects of mass transfer on pulsations and binary evolution in semi-detached configurations.

2.1. Photometry

TESS (Ricker et al. 2015) provides 2-min cadence LCs for all the targets in this study. These LCs were retrieved from the Mikulski Archive for Space Telescopes (MAST) using the LIGHTKURVE package (Lightkurve Collaboration et al. 2018). This short cadence photometry ensures that we detect all the high frequency oscillations, especially beneficial for pulsators like δ Scuti-type variables. LCs obtained from multiple TESS sectors provide a longer time baseline which ensures a good accuracy on the detected frequencies. Photometric 2-min cadence data are summarised in Table 1.

We selected the Simple Aperture Photometry (SAP) flux values for all the targets to avoid distortions in the LCs introduced through Pre-search Data Conditioning (PDC)-SAP fluxes. The data was converted to normalised fluxes and cleaned for long term trends using the wotan Python package (Hippke et al. 2019). LCs of all five targets used in this study are shown in the Figure 1.

2.2. High Resolution Spectra

For the calculation of RVs and determination of atmospheric parameters we used high-resolution spectra, obtained with various spectrographs. Their summary is given in Table 1.

Most of the spectra used for analysis were taken with the FEROS spectrograph (Kaufer et al. 1999), attached to the MPG-2.2 m telescope in La Silla. With an image slicer this instrument provides a resolution of \sim 48000. Data were reduced with the CERES pipeline (Brahm et al. 2017), which provides wavelength-calibrated and barycenter-corrected spectra. We used 20 echelle orders, spanning 4135–6500 Å.

Second important source of data was the CHIRON spectrograph (Tokovinin et al. 2013), attached to the 1.5 m SMARTS telescope installed at Cerro Tololo Inter-American Observatory (CTIO). Aiming for higher efficiency, the spectrograph was used in the fiber mode, providing a resolution of \sim 28000. Extracted and wavelength-calibrated spectra were obtained with the pipeline developed at Yale University (Tokovinin et al. 2013) and provided to the user. However, barycentric velocity corrections were done in-house using the *bvcvcor* procedure within IRAF (Tody 1986). About forty echelle orders (4500–6500 Å) were combined and continuum normalised (in IRAF) to be used for RV and spectral analysis.

One system, TIC 10756751 = GP Cet, has been additionally observed with two other facilities: the HIDES spectrograph ($R \sim$ 55000; Izumiura 1999), attached to the OAO-188 telescope of the Okayama Astronomical Observatory (Japan), and the IRCS camera/spectrograph ($R \sim$ 18000; Kobayashi et al. 2000) behind the Subaru telescope, located at Maunakea (Hawaii). Data reduction and analysis are described in details in Helminiak et al. (2016) and Helminiak et al. (2019) for HIDES and IRCS, respectively.

3. Spectroscopy

RV measurements are essential for estimating the dynamical masses of stars. These RVs, derived from the Doppler shifts of spectral lines in observed spectra, directly reflect the stars’ orbital motions. Additionally, estimates of effective temperature

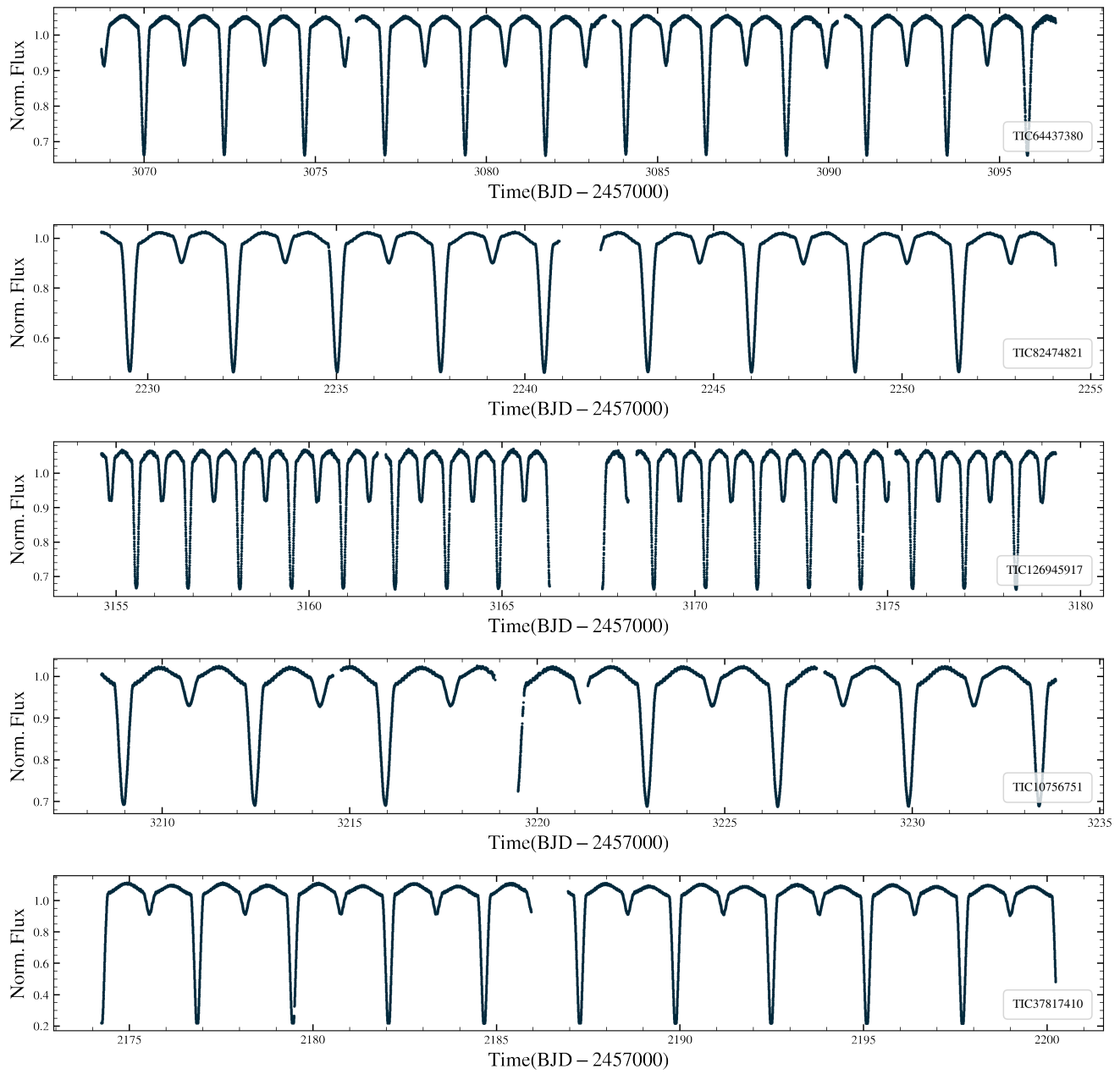


Fig. 1: Short (2-min) cadence LCs of the targets, each for a single TESS sector.

Table 1: Basic information about the targets.

TIC ID	Other ID	TESS sectors with 2-min Photometry	RA (deg., ep=J2000)	Dec (deg., ep=J2000)	V_{mag}	GDR3 ^a dist. (pc)	Spectrograph(s) ^b	No. of Spectra
TIC 64437380	HD 139774	39, 65	235.698351	-57.510948	10.40	458.316	2F	12
TIC 82474821	SW Pup	34, 35, 61, 62	124.712039	-42.753144	9.09	314.257	2F+1C	9+6
TIC 126945917	HD 202042	1, 27, 28, 68	318.732362	-43.3954479	10.15	310.366	2F+1C	9+5
TIC 10756751	GP Cet	3, 42, 43, 70	9.229711	-5.874033	9.90	481.023	1C+OH+SI+2F	8+7+2+1
TIC 37817410	TZ Eri	5, 32	65.418044	-6.019222	9.61	299.643	1C	7

^(a) Gaia Data Release 3 (GDR3; [Gaia Collaboration et al. 2023](#)).^(b) 1C: SMARTS 1.5-m/CHIRON, 2F: MPG-2.2m/FEROS, OH: OAO-188/HIDES, SI: Subaru/IRCS.

and surface gravity obtained from spectral analysis serve as valuable cross-checks for parameters such as flux ratios and relative radii derived from LC modelling.

3.1. Radial Velocities

To calculate the RV values, we used the two-dimensional cross-correlation technique implemented in the `todcor` program ([Zucker & Mazeh 1994](#)). Synthetic spectra used as templates were calculated using the `ATLAS9` model atmosphere ([Ku-](#)

rucz 1979). Errors were calculated using a bootstrap approach (Helminiak et al. 2012).

Orbital solutions for the extracted RVs were calculated using v2FIT (Konacki et al. 2010). The routine estimates the orbital parameters of a double-Keplerian orbit fitted to the data, using a Levenberg-Marquardt scheme. In case of TIC 82474821, a clear Rossiter-McLaughlin effect (Rossiter 1924) was observed. We choose to discard the RVs affected by this to improve the orbital solution.

In general, we fit for the orbital period, P_{orb} , time of periastron passage T_p , systemic velocity, γ , velocity semi-amplitudes, $K_{1,2}$, eccentricity, e and longitude at periastron passage, ω . However, in this work we could omit the last two parameters, as the orbits were found to be circular ($e = 0$) in preliminary fits. The orbital fits are displayed in Fig. 2. The less massive star in all the cases is also much fainter and hence displays larger errors in the derived RV values.

3.2. Broadening functions

In the context of spectral disentangling and fitting, we resorted to broadening functions (BFs), mainly to obtain two necessary parameters: the rotational velocities of the stars and their light contributions. The BF depicts the spectral profiles in velocity space, containing the signatures of RV shifts across various lines, along with intrinsic stellar phenomena such as rotational broadening, spots, and pulsations (Rucinski 1999). The implementation of this method is described in detail in Moharana et al. (2023).

For all five cases, the flux contribution from the fainter secondary is much smaller than from the primary. The noisy nature of the BFs for the secondary components forced us to use this analysis only for the primary stars. The rotational velocities for the primary components are provided in Table 2.

3.3. Spectral disentangling and analysis

The observed spectrum can be disentangled into the individual spectra of both stars, allowing for independent analysis of their atmospheric parameters. One approach is to obtain spectra at different orbital phases, where Doppler shifts cause each star's spectrum to shift within the composite spectrum. By combining multiple spectra with their associated radial velocities (RVs), it is possible to reconstruct the individual component spectra without relying on templates.

Spectral disentangling becomes challenging when phase coverage is sparse or when one component is significantly fainter, leading to a lower signal-to-noise ratio (S/N). Unfortunately, this applies to all targets in our sample. As a result, we could not estimate the light ratio using BFs. Instead, we calculated the passband luminosities for both components in our LC model (see Sect. 4) and used their light ratio for the disentangling process.

We performed spectral disentangling using the DISENTANGLING_SHIFT_AND_ADD code (Shenar et al. 2020, 2022) over the 500–580 nm wavelength range. This selection avoided broad-wing features while ensuring the presence of sufficient narrow lines with adequate S/N. The used RV semi-amplitudes were obtained with v2FIT. For further analysis, we proceeded with only the disentangled primary spectrum, continuum-corrected using the SUPPNET package (Różański et al. 2022)¹.

3.4. iSPEC

We used the iSPEC framework (Blanco-Cuaresma et al. 2014; Blanco-Cuaresma 2019) to determine the astrophysical parameters of the disentangled primary spectrum. If necessary, minimal continuum normalization was performed within iSPEC using third-order splines, and slight RV shifts were also corrected.

From the multiple options provided by iSPEC for spectral fitting we use the ability to generate synthetic spectra on the go using several choices of radiative transfer codes. Specifically, we chose SPECTRUM (Kaufer et al. 1999) for its speed and accuracy along with ATLAS9 plane-parallel model atmospheres (Kurucz 2005). We used the line lists from the Gaia-ESO Survey covering the wavelength range 420–920 nm, and solar abundances from Asplund et al. (2009). iSPEC uses χ^2 minimization to choose the best-fit from the ones generated by SPECTRUM and the observed spectra.

During the fitting process, we fix the spectral resolution to the instrumental value, and $\log(g)$ to the value from LC modelling (Sect. 4) to minimise the degeneracy in fitted values. We perform the fitting procedure using the line lists best suited for determining atmospheric parameters (provided within iSPEC) and we fit for T_{eff} , $v \sin(i)$ and microturbulent velocity (v_{mic}). The limb-darkening coefficients are adapted from Claret (2017).

3.5. Grid Search in Stellar Paramters (GSSP)

In order to verify the secondary temperatures obtained using the temperature ratio parameter values from the LC fitting results (Sect. 4), we use the GSSP_COMPOSITE module of the Grid Search in Stellar Paramters (GSSP) software package (Tkachenko 2015). It uses the method of atmosphere models and spectrum synthesis, which performs a comparison of the observations with theoretical spectra from the grid. These synthetic spectra are calculated using the SYNTHEV LTE-based radiative transfer code (Tsymbal 1996) and a grid of atmospheric models pre-computed using LLMODELS (Shulyak et al. 2004).

We initiate the primary temperature at the value estimated using iSPEC and fit for the T_{effs} , $v \sin(i)$, and (v_{mic}). The best-fit values of the parameters are mentioned in Table 2. The errors are assumed to be the step-size of the parameter grid used to generate the synthetic spectra. The spectral fits are shown in Figure 3.

4. Light curve modelling

Stars in binaries with short orbital period influence each other with significant gravitational forces. These strong tidal forces cause ellipsoidal deformations that are visible in their LCs. These effects can be modelled precisely using the Roche geometry (Eggleton 1983b). This treatment also allows to calculate if the stars will fill their respective Roche lobe beyond the point at which mass of the star is no longer gravitationally bound to it. This allows for reproducing accurate semi-detached and contact binary configurations and their observational signatures in LCs.

The PHOEBE2 (Prša et al. 2016; Horvat et al. 2018; Comroy et al. 2020) incorporates the Roche geometry to model EBs. It also provides treatment for limb darkening laws, third light, and stellar spots, making it physically precise and thus suitable for modelling the high-precision TESS LCs of oEAs.

However, if one or both the stars in the EB harbor rapidly evolving spots, the process of obtaining a binary model becomes more challenging. This prevents us from having a single model for all the sectors as the spot parameters may affect the stellar and

¹ <https://github.com/RozanskiT/suppnet>

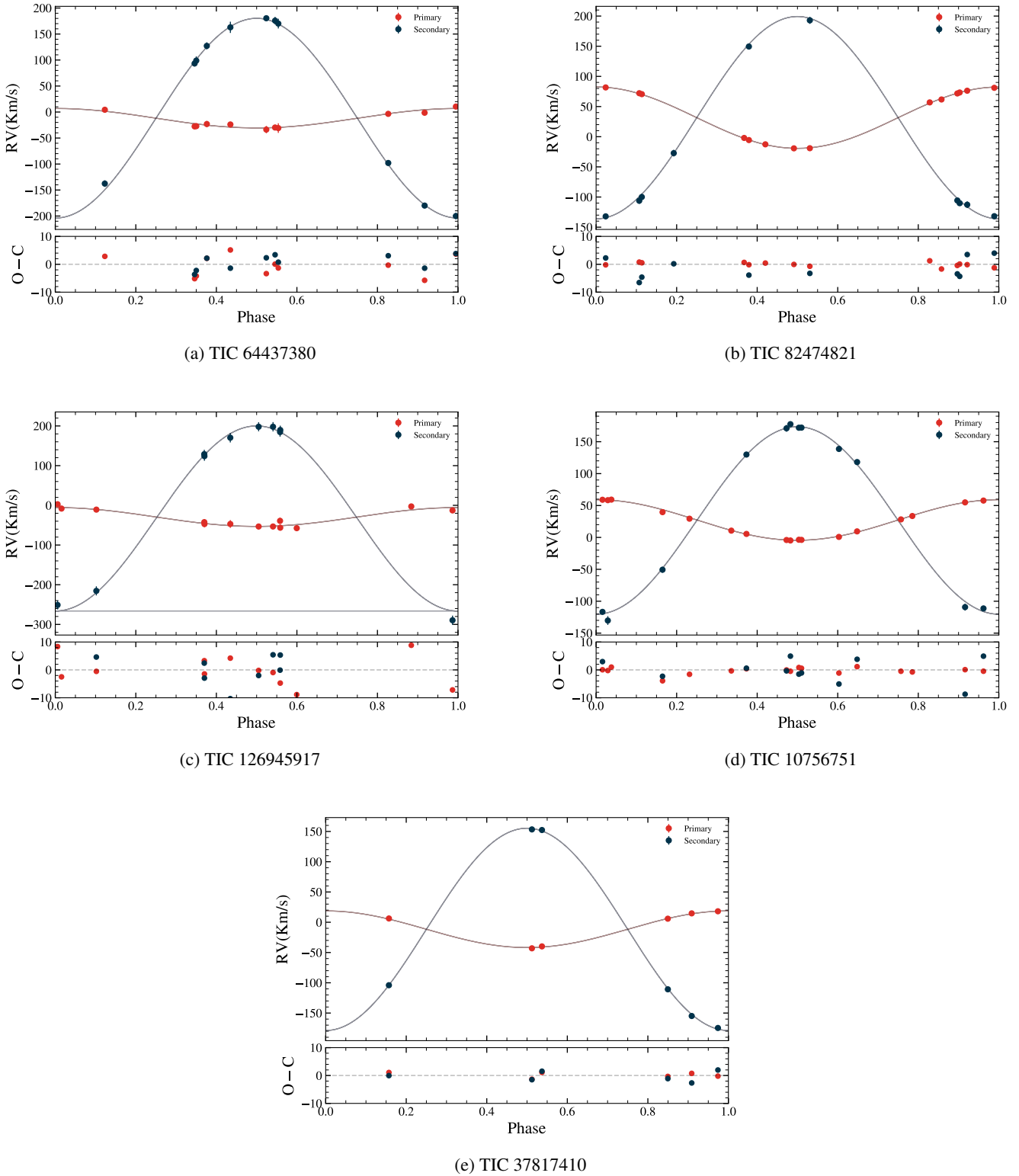


Fig. 2: Orbital fits obtained for the RV curves for the targets. Here, primary refers to the more massive star and secondary is the less massive companion. The phase 0 is set to the time of the first quadrature for circular orbits.

orbital parameter values if not taken into account. All the systems show signs of activity in the observation window. For each target we initially select the sector where minimal spot activity in the form of the O'connell effect (Roberts 1906; O'Connell

1951; Milone 1968) is visible in the LCs. We use these LCs to calculate our primary model.

We set the mass ratio (q) and the projected semi-major axis $a \sin(i)$ to the values obtained from the RV solutions. The limb darkening coefficients are determined according to the study by

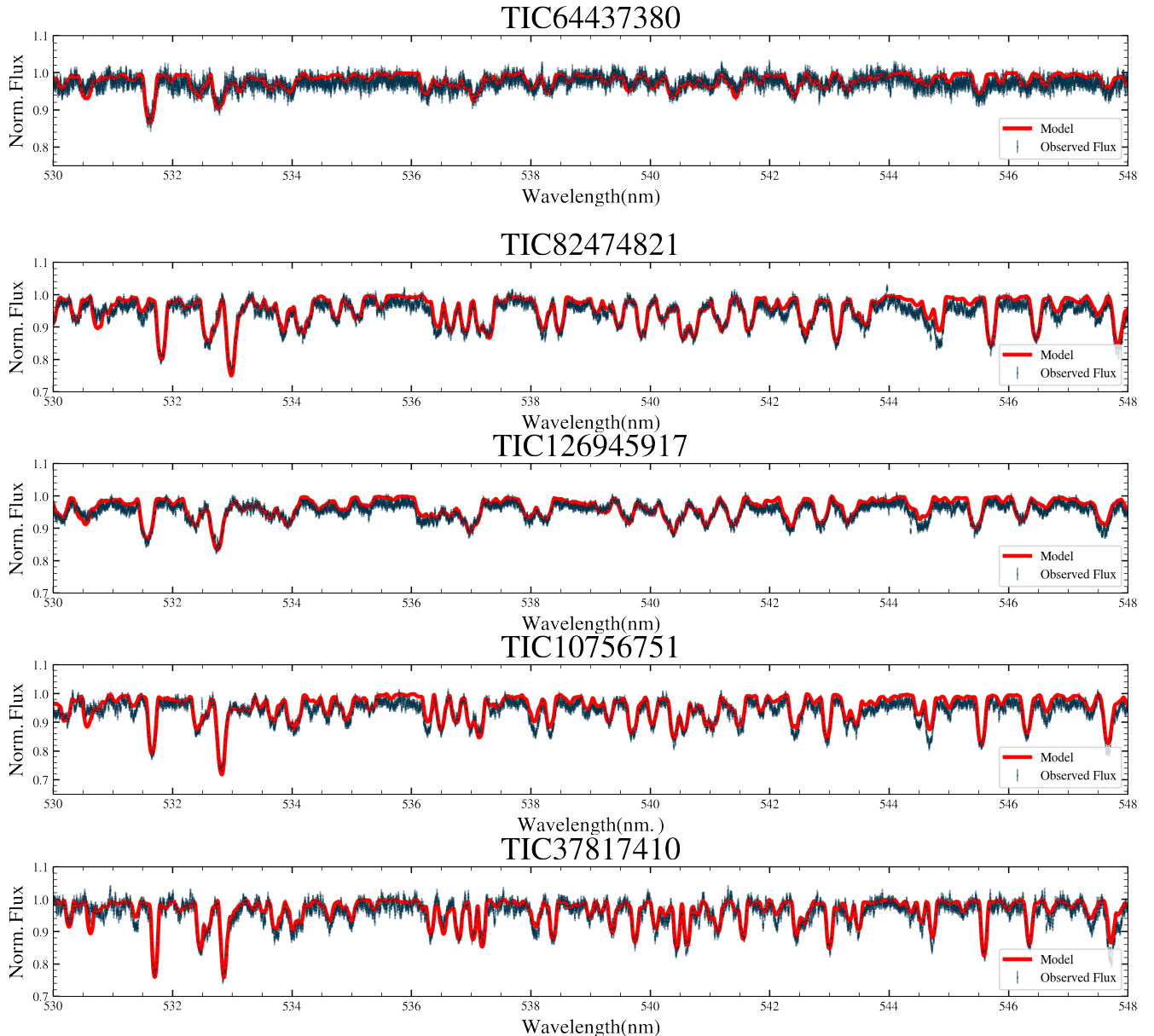


Fig. 3: Observed composite spectrum (blue) of the superimposed targets with the GSSP model spectrum (in red) corresponding to the atmospheric parameters from Table 2.

Claret (2017), while the gravity darkening coefficients are set to 1 for the primary star with radiative envelope and 0.32 for the secondary star with convective envelope. We found that using 2500 triangles to discretize the surface of each star was a good balance between accuracy and computational efficiency.

When constructing the forward model, we apply the semi-detached constraint provided in the code, ensuring that the equivalent radius reaches its maximum value, corresponding to the star filling its Roche lobe. The forward model was then optimised using a combination of Nelder-Mead and Differential Evolution optimizers within PHOEBE2. The fitted parameters include the radii ratio, effective temperature ratio, passband luminosity, and orbital inclination.

In some cases while using semi-detached configuration, we encountered convergence issues at the edge of the Roche tails. To mitigate these errors, we switched to a detached configuration, setting the radius of the secondary star as close as possible to the value of largest possible equivalent radius constrained by

the Roche configuration – without triggering errors – before proceeding with the optimization runs.

The errors were estimated using the Markov Chain Monte Carlo (MCMC) sampling, implemented in PHOEBE2 via the EMCEE sampler (Foreman-Mackey et al. 2013). The primary parameters for which we assessed uncertainties included ratio of the stellar radii, inclination, passband luminosity, and the temperature ratio. We show the results in figure 4 and Table 2.

5. Eclipse Timing Variations

Eclipse timing variations in eclipsing binary star systems may arise from several dynamical factors. For example, large-scale mass transfer events can alter the orbital momentum, while the gravitational influence of a tertiary companion can perturb the binary's orbit. Additionally, stellar spots can induce timing variations; in such cases, the O-C diagram of the eclipse minima

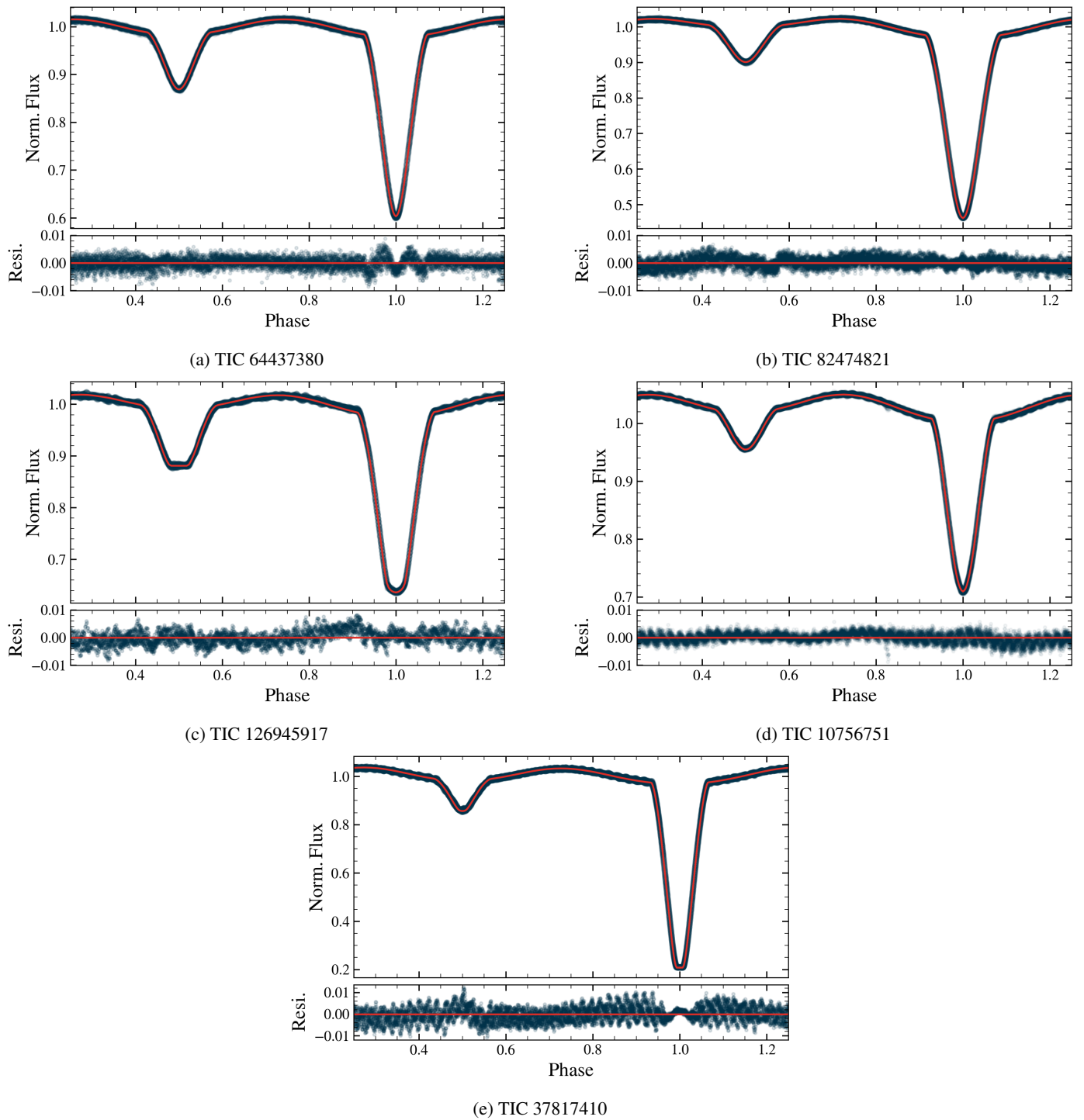


Fig. 4: The results of LC modelling of the systems using the PHOEBE2 software. Upper panel(s): Phased TESS LC (blue) with the best-fitting model superimposed (red). Lower panel(s): Residuals from the fitting procedure.

typically shows an anti-correlation between the primary and secondary eclipses.

To search for potential signs of active mass transfer in our systems, we examined the O–C variations. For this purpose, we determined the times of the primary and secondary eclipse minima (see Appendix A) using the method developed by Marcadon & Prša (2024). Since historical minima timing data are unavailable for our targets, this analysis is based solely on the available TESS observations. The O–C values are computed using the fol-

lowing equation:

$$\Delta_{\text{obs}} = T_{\text{obs}}(E) - (T_0 + E \cdot P),$$

where T_0 is the adopted initial epoch for each dataset (indicated in the tables as Cycle 0), P is the orbital period, and E is the cycle number.

For TIC82474821 and TIC126945917, we observed a slight anti-correlation between the O–C values of the primary and secondary eclipse timings, suggesting that brightness asymmetries – likely due to stellar spots – are present. However, due to the

Table 2: Parameters of the five oEA systems obtained using a combination of LC modelling and spectral analysis. In some cases we mention the method used to determine the parameters in the “()” bracket alongside the parameter name.

Parameters	TIC 64437380	TIC 82474821	TIC 126945917	TIC 10756751	TIC 37817410
T_0 (BJD-2457000)	2363.57069 ± 0.0002	2232.26734 ± 0.0005	3155.52250 ± 0.00001	3208.97018 ± 0.00002	1439.30929 ± 0.00045
P_{orb} [days]	2.34694 ± 0.00019	2.74738 ± 0.00001	1.34109 ± 0.00002	3.48827 ± 0.00019	2.60611 ± 0.00640
i [$^{\circ}$]	82.95 ± 0.15	79.95 ± 0.01	89.10 ± 0.19	75.40 ± 0.05	87.30 ± 0.01
q	0.098 ± 0.017	0.303 ± 0.014	0.102 ± 0.017	0.217 ± 0.009	0.181 ± 0.008
K_1 [km s $^{-1}$]	18.7 ± 2.5	50.9 ± 0.5	23.8 ± 2.9	31.8 ± 0.4	30.3 ± 1
K_2 [km s $^{-1}$]	192.1 ± 4.2	167.8 ± 2.4	233.2 ± 6.2	146.9 ± 1.8	167.1 ± 1.4
γ [km s $^{-1}$]	-11.9 ± 1.6	31.56 ± 0.4	-29.3 ± 2.4	27.3 ± 0.3	-11.5 ± 0.7
$v \sin(i)_1$ [km s $^{-1}$] (BF)	74 ± 7	57 ± 1	78 ± 1	52 ± 2	45 ± 2
a [R $_{\odot}$]	9.782 ± 0.225	11.875 ± 0.133	6.815 ± 0.181	12.327 ± 0.125	10.171 ± 0.085
$T_{\text{eff},1}$ [K] (iSPEC)	8450 ± 210	7450 ± 100	7780 ± 120	7300 ± 130	7920 ± 150
$T_{\text{eff},2}$ [K] (GSSP)	5900 ± 200	4400 ± 200	5100 ± 200	4500 ± 200	4800 ± 200
$T_{\text{eff},2}/T_{\text{eff},1}$	0.653 ± 0.001	0.569 ± 0.001	0.709 ± 0.005	0.635 ± 0.005	0.554 ± 0.001
M_1 [M $_{\odot}$]	2.14 ± 0.14	2.39 ± 0.09	2.15 ± 0.17	1.87 ± 0.06	1.76 ± 0.04
M_2 [M $_{\odot}$]	0.208 ± 0.033	0.725 ± 0.019	0.219 ± 0.033	0.406 ± 0.011	0.319 ± 0.012
R_1 [R $_{\odot}$]	2.685 ± 0.010	3.026 ± 0.005	1.989 ± 0.001	3.244 ± 0.015	1.761 ± 0.001
R_2 [R $_{\odot}$]	1.95 (fixed)	3.20 (fixed)	1.24 (fixed)	3.19 (fixed)	2.6 (fixed)
$\log(g)_1$	3.940 ± 0.002	3.822 ± 0.001	4.035 ± 0.004	3.715 ± 0.001	4.202 ± 0.002
$\log(g)_2$	3.143 ± 0.004	3.232 ± 0.005	3.458 ± 0.002	3.027 ± 0.001	3.165 ± 0.005

limited data spanning only a short time period, no definitive conclusions could be drawn regarding the mass-transfer rate.

6. Binary evolution

The process of mass-transfer changes the most important characteristic feature of a star that determines its evolution. The state of the stars in an Algol-type system is not representative of the evolution that a similar mass star would go through. The acceptor not only gains the extra mass but also, in that process, goes through a change in the structure and composition of its outer layers. This process also changes the orbital configuration of the binary system by means of change in angular momentum.

In order to account for these effects, theoretical modelling needs to consider the binary interaction while evolving such system of stars. To perform such binary stellar evolution we used the MESA-BINARY module within the MESA code (Modules for Experiments in Stellar Astrophysics, Paxton et al. 2011, 2013, 2015, 2018, 2019; Jermyn et al. 2023, version 23.05.1) to construct models under the non-rotating approximation.

The MESA code builds upon the efforts of many researchers who advanced our understanding of physics and relies on a variety of input microphysics data. The MESA EOS is a blend of the OPAL (Rogers & Nayfonov 2002), SCVH (Saumon et al. 1995), FreeEOS (Irwin 2004), HELM (Timmes & Swesty 2000), and PC (Potekhin & Chabrier 2010) EOSes. Radiative opacities are primarily from the OPAL project (Iglesias & Rogers 1993, 1996), with data for lower temperatures from Ferguson et al. (2005) and data for high temperatures, dominated by Compton-scattering from Buchler & Yueh (1976). Electron conduction opacities are from Cassisi et al. (2007). Nuclear reaction rates are from JINA REACLIB (Cyburt et al. 2010) plus additional tabulated weak reaction rates from Fuller et al. (1985), Oda et al. (1994) and Langanke & Martínez-Pinedo (2000). Screening is included via the prescription of Chugunov et al. (2007). Thermal neutrino loss rates are from Itoh et al. (1996). The MESA-BINARY module allows for the construction of a binary model and the simultaneous evolution of its components, taking into account several important interactions between them. In particular, this module incorporates angular momentum evolution due to mass transfer. Roche lobe radii in binary systems are computed using the fit of Eggleton (1983a). Mass transfer rates in Roche lobe

overflowing binary systems are determined following the prescriptions of Ritter (1988) and Kolb & Ritter (1990).

In order to reproduce the evolution of the system, we built an extensive grid of evolutionary models. We constructed a set of varying parameters, i.e. initial orbital period, initial masses of the components, metallicity, overshooting from the convective core, mixing-length theory scaling coefficient and a fraction of mass lost during MT, with the ranges as given in Table 3. From this set we constructed vectors of initial parameters with the assumed numerical accuracy (see last column of Table 3) and calculated the evolutionary tracks. The parameters were chosen randomly from uniform distributions within the given ranges. All of these parameters were chosen independently of others, except for the masses. The masses were varied between $0.5 M_{\odot}$ and $2.5 M_{\odot}$, ensuring that the mass of the primary star was larger than that of the secondary. We tested the rate of the mass transfer loss from the system as a fraction of mass that is lost from the vicinity of the accretor in a form of a fast wind during MT, in the range from $\beta = 0.0$ to $\beta = 0.3$. We used Kolb & Ritter (1990) mass transfer prescription and assumed a constant eccentricity $e = 0$ throughout the system’s evolution. Initial orbital periods in our models were chosen from 1.2 to 5 days.

Table 3: Summary of the parameter ranges and sampling precision used in the evolutionary modeling of the five oEA systems. The table lists each parameter, its minimum and maximum values, and the precision with which it was sampled from a uniform distribution.

Parameter	Range	Accuracy
Initial orbital period, P_{ini} [d]	1.2 - 5.0	10^{-5}
Initial masses, $M_{\text{don/acc,ini}}$ [M $_{\odot}$]	0.5 - 2.5	10^{-3}
Metallicity, Z	0.01 - 0.03	10^{-3}
Convective-core overshooting, f_{ov}	0.001 - 0.030	10^{-3}
Mixing-length theory parameter, α_{MLT}	0.5 - 1.8	10^{-1}
Fraction of mass lost during MT, β	0.0 - 0.3	10^{-1}

In our evolutionary computations, we used the AGSS09 (Asplund et al. 2009) initial chemical composition of the stellar matter and the OPAL opacity tables. These tables were supplemented with data from Ferguson et al. (2005) for lower temperatures. For higher temperatures, hydrogen-poor or metals-rich conditions we used C and O enhanced tables. To determine the chemical composition of stars we varied the value of metallicity Z, from 0.01 to 0.03 and used the linear scaling relations (e.g.,

[Choi et al. 2016](#)):

$$Y = Y_p + \left(\frac{Y_{\text{protosolar}} - Y_p}{Z_{\text{protosolar}}} \right) Z,$$

with primordial helium abundance $Y_p = 0.249$ ([Planck Collaboration et al. 2016](#)), and $Y_{\text{protosolar}} = 0.2703$, $Z_{\text{protosolar}} = 0.0142$ proto-solar abundances ([Asplund et al. 2009](#)).

Convective instability was treated using the Ledoux criterion, combined with the mixing length theory based on the [Henyey et al. \(1965\)](#) model, employing a mixing-length parameter between $\alpha_{\text{MLT}} = 0.5$ and $\alpha_{\text{MLT}} = 1.8$. In regions that were stable according to the Ledoux criterion but unstable by the Schwarzschild criterion, we applied semi-convective mixing using a scaling factor of $\alpha_{\text{sc}} = 0.1$, following the formalism of [Langer et al. \(1985\)](#). To address regions exhibiting inversion in the mean molecular weight, such as those formed during mass accretion, we applied thermohaline mixing using the formalism of [Kippenhahn et al. \(1980\)](#), with an $\alpha_{\text{th}} = 1$ coefficient. As our models did not include rotational mixing, we introduced a minimum diffusive mixing coefficient of $D = 10 \text{ cm}^2 \text{ s}^{-1}$ to smooth out numerical noise or discontinuities in internal profiles. Additionally, we accounted for overshooting beyond the formal convective boundaries, using an overshooting parameter, f_{ov} , to capture turbulent motions extending into the radiative zone. We applied an exponential overshooting scheme by [Herwig \(2000\)](#) on the top of the H-burning core with changing value from $f_{\text{ov}} = 0.001$ to $f_{\text{ov}} = 0.03$.

We also account for the effects of stellar winds. Our models include wind mass loss, based on the prescriptions of [Vink et al. \(2001\)](#), [Reimers \(1975\)](#) and [Blöcker \(1995\)](#), depending on the effective temperature and the evolutionary stage of a star. For these prescriptions, we adopt efficiency coefficients of $\eta_V = 0.1$, $\eta_R = 0.5$, and $\eta_B = 0.1$, respectively.

Our intention was to apply the aforementioned grid to all systems analysed in this paper. To achieve this, we established a comprehensive grid of 5 000 models, calculated based on the parameter ranges outlined in Table 3. This grid served as a foundation for our analysis, allowing us to explore a wide spectrum of stellar configurations. From this initial grid, we carefully selected time steps for each system, that correspond to the values of the measured orbital periods within errors. To select the best fits between the observed and theoretical values we calculated the Mahalanobis distance ([Mahalanobis 1936](#)) for each selected time step for the masses and radii. Then, for each system we selected models whose values deviated by up to 50% from the observed equivalents, in order to extract a sample of models that enabled us to constrain the ranges of the initial parameters. This approach led to the creation of additional grids, incorporating models computed for narrower ranges with more stringent error thresholds, up to 10%. We summarize the effects of evolutionary computations for each system in Table 4 and Figure 5. The orange and blue lines denote the evolutionary tracks for the acceptor and donor, respectively, with dots overplotted on each track, to mark the locations of the best-fitting timestamps. The observed positions are indicated by the error boxes. The lower panels display the evolution of masses, radii and the orbital period with the x-axes representing the evolutionary time (τ) normalized to the current age (τ_{sys}) of the corresponding best-fit model. We also provide short descriptions of the results below.

TIC 82474821: We have identified 16 models that match the observed parameters within 10% of its components' masses and radii. Some solutions suggest Case A MT, but the majority indicates that the system was formed via non-conservative case B

MT, and is 0.5–3 Gyr old. During the evolution, the initially less massive component accretes mass from its companion, leading to mass ratio reversal and to expansion of the convective core. The donor models align at the ridge of the ending phase of mass transfer, after the exhaustion of core hydrogen, and before the onset of hydrogen burning in the envelope. Depending on the MT case, the accretor models point to either early stages of core rejuvenation (case B, central hydrogen abundance increases to approx. 0.7) or much later stages of evolution, with $H \approx 0.2 – 0.3$ in the case of type A mass transfer.

TIC 10756751: All of the models we were able to find fit within 15% of the measured masses and radii of the components. According to these models, TIC 10756751 is likely to have been created from a binary with relatively small orbit, with $P_{\text{orb}} \approx 1.2 – 1.6 \text{ d}$, via almost conservative case A mass transfer, with up to 10% of transferred mass lost from the system. The system is relatively old, i.e. 1.86 – 8.13 Gyr, with the accretor close to terminal age main sequence (TAMS; $H \approx 0.03 – 0.3$), and the donor close to becoming a helium-core pre-white dwarf.

TIC 37817410: We have found 13 models that fit within 15% of the measured masses and radii of the components, and point to $\tau_{\text{sys}} \approx 1.3 – 11.2 \text{ Gyr}$. The initial conditions of TIC 37817410 binary are unclear, as wide ranges of initial orbital periods (1.2 – 2.5 d) and initial masses ($1 – 1.83 M_{\odot}$ for the donor, $0.5 – 0.9 M_{\odot}$ for the accretor) are possible. However, some of the best fitting models, point to the over-solar metallicities. In these models, the donor, after transferring a substantial amount of mass to its companion, undergoes an unstable CNO burning cycle in its envelope. This process results in a series of outbursts, occasionally causing the donor to exceed its Roche lobe and triggering brief episodes of additional mass transfer to the companion.

TIC 64437380 and TIC 126945917: The best evolutionary models that we were able to identify for TIC 64437380 and TIC 126945917 fit only up to 50% of the components' masses and radii. We believe that the difficulties in obtaining better fits arise from the parameter ranges chosen for calculating evolutionary tracks, particularly the value of the initial orbital period for the former system and secondary's initial masses for the latter system (see Table 3). The models we found cluster near the lower limits of the assumed orbital period and masses of the secondary, and the resulting classification of the mass transfer as type B seems to support our hypothesis. We consider that lowering the lower limit of P_{orb} and $M_{\text{acc,ini}}$ could lead to the identification of additional models with case A mass transfer, which might improve the overall quality of the fits.

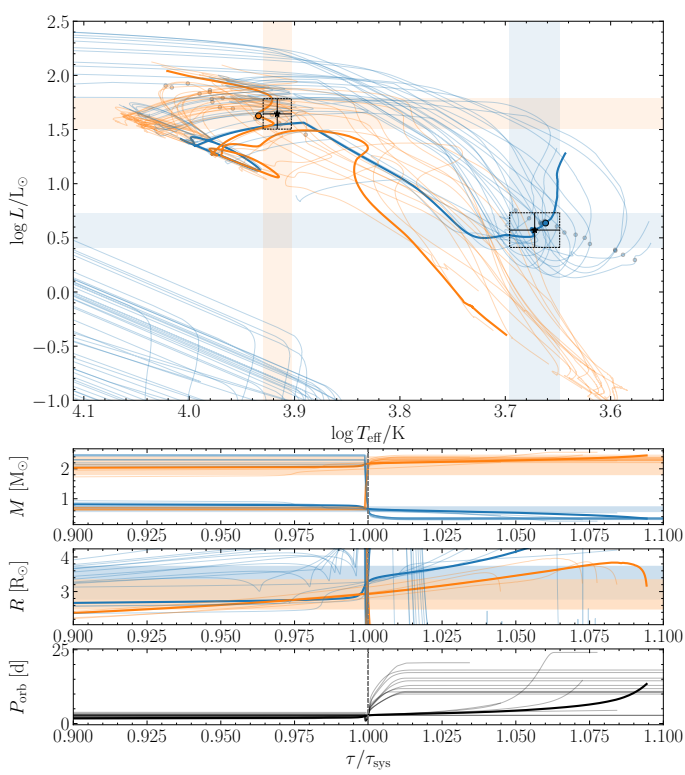
The overall analysis supports the general evolutionary type of each system presented in this paper. After mass transfer starts in, either, case A or B scenario, the initially less massive accretor gains mass, builds and expands its convective core. On the other hand, the donor after losing a significant fraction of its mass still retains sufficiently thick hydrogen envelope to enter the red giant phase, after which the turbulent CNO burning will cause a series of outbursts, completely washing-out any hydrogen left to, eventually, become a He white dwarf.

7. Pulsation Analysis

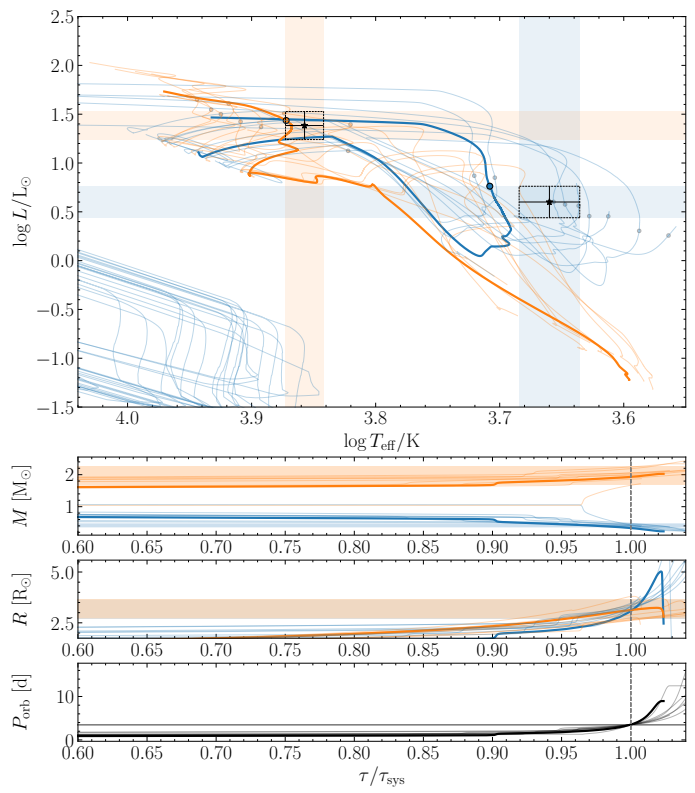
To determine the pulsation frequencies for each system, we use the residuals left after subtracting the binary model from the LC. To ensure a good frequency resolution we recalculated binary models for the multiple TESS sectors obtaining the longest temporal baseline possible. The binary model is almost never perfect; as the LCs are affected due to spots and pulsations. To ensure that we have minimum contamination from the binary sig-

Table 4: The results of the evolutionary computations summarizing the initial and final parameters of the models. The models are sorted by fit quality.

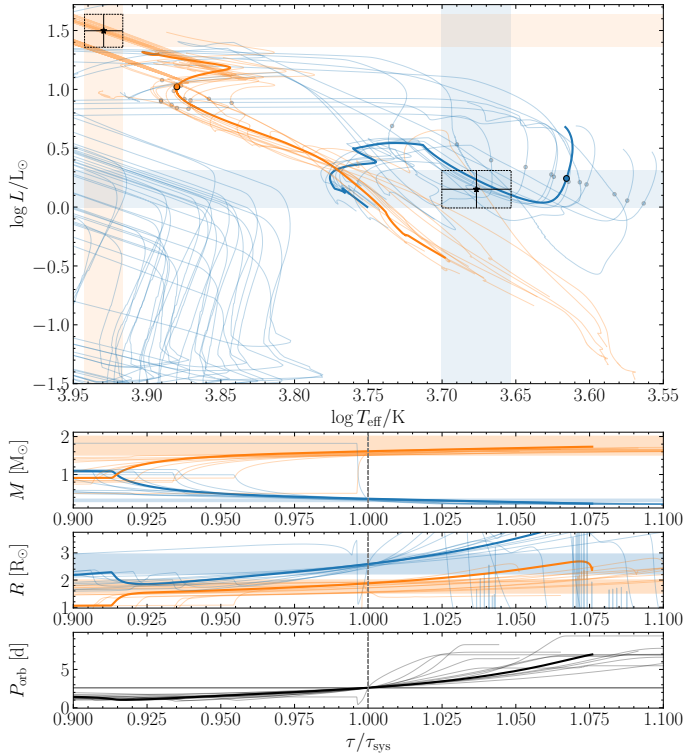
Mod. #	P_{ini} [d]	INITIAL PARAMETERS						FINAL PARAMETERS						MT Case	
		$M_{\text{don,inj}}$ [M_{\odot}]	$M_{\text{acc,inj}}$ [M_{\odot}]	Z	f_{ov}	α_{MLT}	β	M_{acc} [M_{\odot}]	R_{acc} [R_{\odot}]	$\log T_{\text{eff}}^{\text{acc}}$	M_{don} [M_{\odot}]	R_{don} [R_{\odot}]	$\log T_{\text{eff}}^{\text{don}}$	$\log \tau_{\text{sys}}$	
TIC 82474821															
1	1.36039	2.061	0.958	0.028	0.022	1.3	0.13	2.169	2.931	3.934	0.66	3.289	3.662	9.19	A
2	2.97347	2.099	0.629	0.030	0.027	1.5	0.02	2.041	2.878	3.99	0.651	3.29	3.69	8.96	B
3	1.33773	2.148	0.964	0.017	0.014	0.5	0.19	2.162	2.964	3.914	0.661	3.284	3.577	9.18	A
4	1.26583	1.552	1.140	0.025	0.023	0.8	0.03	1.995	2.947	3.889	0.66	3.288	3.588	9.47	A
5	2.69152	2.204	0.709	0.010	0.018	1.1	0.11	2.055	2.863	3.979	0.687	3.348	3.663	8.91	B
6	3.79526	2.465	0.620	0.028	0.011	1.0	0.21	2.041	3.04	4.001	0.662	3.311	3.633	8.7	B
7	2.39379	2.481	0.715	0.014	0.015	1.0	0.26	2.089	2.781	3.978	0.62	3.23	3.667	8.78	B
8	3.10770	2.152	0.657	0.014	0.010	0.7	0.06	2.028	2.839	3.958	0.689	3.349	3.596	8.93	B
9	1.30167	1.922	0.933	0.018	0.027	1.5	0.02	2.199	2.812	3.937	0.62	3.214	3.678	9.33	A
10	3.17406	2.312	0.663	0.013	0.008	0.9	0.16	2.032	3.036	3.968	0.679	3.335	3.625	8.83	B
11	3.45509	2.293	0.630	0.022	0.002	0.8	0.15	2.006	3.058	3.98	0.67	3.321	3.596	8.78	B
12	2.51167	2.427	0.694	0.026	0.015	0.9	0.24	2.065	3.119	3.98	0.619	3.231	3.644	8.75	B
13	2.66580	2.437	0.717	0.017	0.011	1.1	0.17	2.176	2.726	4.016	0.676	3.327	3.651	8.78	B
14	2.94571	2.456	0.638	0.027	0.015	1.1	0.16	2.174	2.697	4.022	0.623	3.239	3.665	8.73	B
15	1.43394	1.986	0.837	0.023	0.027	1.2	0.03	2.171	3.136	3.921	0.6	3.184	3.666	9.28	A
16	2.55736	2.303	0.662	0.024	0.009	0.9	0.22	1.987	2.719	3.971	0.6	3.196	3.62	8.8	B
TIC 10756751															
1	1.23834	1.773	0.574	0.023	0.025	1.6	0.05	1.93	3.13	3.872	0.334	3.061	3.708	9.49	A
2	1.27960	1.980	0.674	0.014	0.027	1.7	0.03	2.185	3.093	3.918	0.411	3.279	3.721	9.37	A
3	1.26999	1.839	0.766	0.013	0.025	0.9	0.06	2.053	3.387	3.874	0.458	3.397	3.636	9.44	A
4	1.23910	2.060	0.813	0.012	0.023	1.6	0.09	2.24	2.884	3.944	0.483	3.457	3.704	9.28	A
5	1.53421	1.918	0.599	0.029	0.023	0.8	0.03	2.051	2.695	3.933	0.412	3.28	3.647	9.27	A
6	1.59119	1.898	0.566	0.025	0.028	0.6	0.05	1.983	2.65	3.925	0.396	3.239	3.657	9.33	A
7	1.29047	1.645	0.633	0.027	0.016	0.8	0.00	1.9	2.644	3.892	0.369	3.16	3.588	9.46	A
8	1.29674	1.066	1.044	0.025	0.024	0.8	0.00	1.668	2.757	3.822	0.433	3.334	3.564	9.91	A
9	1.20346	1.775	0.661	0.019	0.012	1.1	0.04	2.015	2.608	3.909	0.356	3.123	3.628	9.42	A
10	1.24970	1.655	0.747	0.028	0.028	0.9	0.08	1.856	3.795	3.82	0.437	3.345	3.612	9.54	A
TIC 37817410															
1	1.47500	1.093	0.911	0.025	0.006	1.4	0.03	1.613	1.878	3.88	0.363	2.587	3.616	9.84	B
2	1.26929	1.835	0.531	0.023	0.027	1.5	0.29	1.594	1.916	3.89	0.327	2.505	3.734	9.51	A
3	1.25630	1.106	0.899	0.024	0.009	1.2	0.06	1.588	1.788	3.882	0.367	2.597	3.602	9.83	B
4	1.41540	1.827	0.503	0.020	0.011	0.5	0.27	1.578	1.573	3.872	0.35	2.567	3.583	9.11	B
5	1.43283	1.102	0.848	0.017	0.002	0.7	0.02	1.569	1.706	3.875	0.36	2.579	3.563	9.89	B
6	1.23132	1.621	0.555	0.026	0.028	1.4	0.20	1.562	1.925	3.877	0.353	2.567	3.69	9.6	A
7	1.39078	1.096	0.830	0.012	0.007	1.2	0.04	1.551	1.567	3.89	0.339	2.527	3.624	9.89	A
8	1.94405	1.057	0.798	0.012	0.014	1.8	0.00	1.543	1.55	3.89	0.306	2.442	3.667	9.95	A
9	1.23281	1.137	0.842	0.014	0.019	1.3	0.12	1.527	1.528	3.88	0.353	2.564	3.626	9.86	B
10	1.29737	1.120	0.830	0.026	0.005	0.9	0.12	1.516	1.718	3.871	0.335	2.517	3.574	9.8	B
11	2.51667	1.000	0.905	0.016	0.011	1.6	0.07	1.507	1.904	3.843	0.346	2.544	3.643	10.05	A
12	1.21457	1.639	0.610	0.023	0.019	0.8	0.29	1.507	1.846	3.858	0.367	2.598	3.607	9.57	A
13	1.37117	1.115	0.747	0.027	0.005	1.4	0.02	1.505	1.549	3.883	0.336	2.522	3.614	9.79	B
TIC 64437380															
1	1.30566	1.024	0.916	0.019	0.013	1.1	0.08	1.608	2.729	3.806	0.263	2.167	3.612	10.01	A
2	1.26533	0.979	0.871	0.020	0.019	0.5	0.15	1.457	2.334	3.797	0.28	2.214	3.531	10.1	A
3	1.32244	0.989	0.830	0.029	0.011	0.7	0.10	1.466	2.178	3.82	0.275	2.199	3.553	10.0	B
4	2.35677	0.981	0.866	0.014	0.020	1.3	0.14	1.484	1.962	3.835	0.255	2.142	3.641	10.11	B
5	1.31652	0.993	0.706	0.012	0.014	0.8	0.06	1.427	1.651	3.856	0.218	2.034	3.606	10.09	B
6	1.70143	1.046	0.725	0.022	0.005	1.6	0.28	1.303	1.485	3.828	0.237	2.089	3.651	9.95	B
TIC 126945917															
1	1.28362	1.092	0.823	0.024	0.003	0.6	0.09	1.534	2.001	3.845	0.304	1.57	3.551	9.88	B
2	1.38418	1.022	0.728	0.023	0.019	1.6	0.21	1.329	1.488	3.836	0.256	1.481	3.647	9.98	B
3	1.31652	0.993	0.706	0.012	0.014	0.8	0.06	1.337	1.427	3.839	0.316	1.59	3.596	10.06	B
4	2.62958	0.970	0.720	0.016	0.004	1.4	0.30	1.235	1.426	3.805	0.229	1.425	3.662	10.11	B
5	1.39068	1.041	0.555	0.030	0.009	1.7	0.12	1.264	1.387	3.834	0.231	1.43	3.653	9.89	B
6	1.27810	1.081	0.665	0.011	0.021	1.7	0.23	1.293	1.359	3.835	0.26	1.488	3.675	9.92	B
7	1.31712	1.131	0.562	0.018	0.010	1.5	0.24	1.178	1.229	3.795	0.317	1.592	3.639	9.83	B
8	1.56653	1.048	0.525	0.024	0.020	1.6	0.25	1.077	1.104	3.782	0.309	1.579	3.639	9.91	B



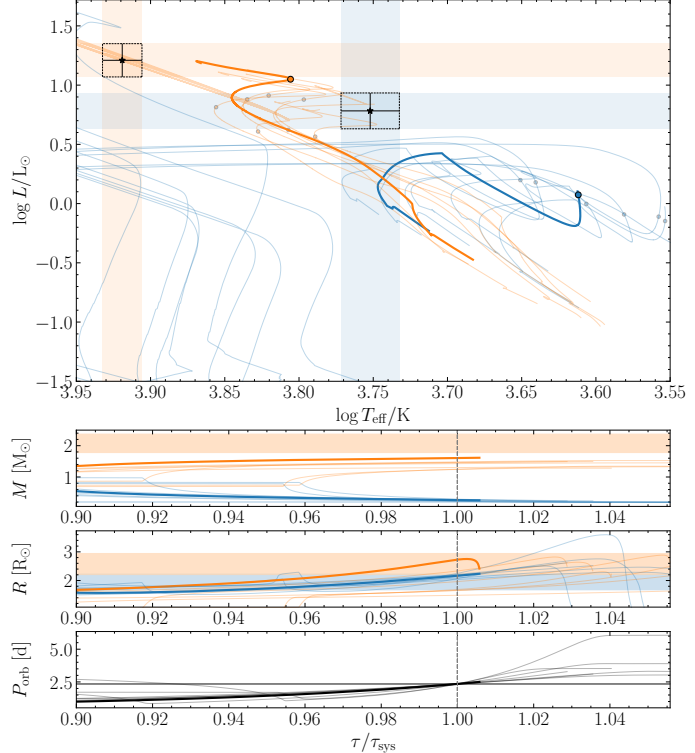
(a) TIC 82474821



(b) TIC 10756751



(c) TIC 37817410

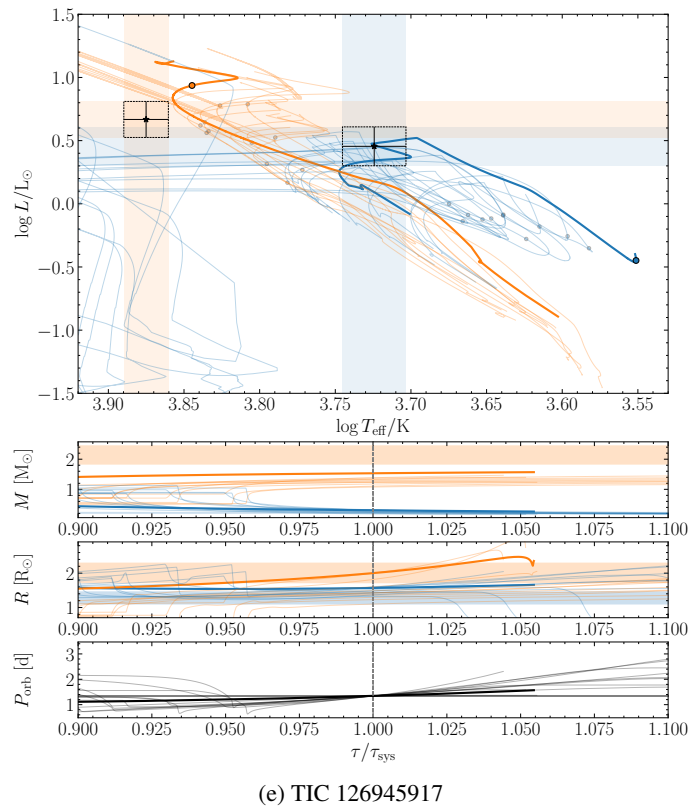


(d) TIC 64437380

nal during the pulsation analysis we further clean the residuals in two steps. Firstly, we clean them for the first 100 harmonics of the orbital frequency. In the next step, we use the WOTAN Python package to remove the long term trends arising due to imperfect subtraction of spot signals and eclipse ingress/egress profiles. In

this step, we chopped off the LCs at the eclipses where the detrending was not sufficient.

To perform the time series analysis on these curated residuals we use v1.2.9 of the PERIOD04, based on Lenz & Breger (2005). We perform the search for oscillation frequencies from 0 to 80



(e) TIC 126945917

Fig. 5: The HR diagrams and the evolution of masses, radii, and orbital period for the best-fit evolutionary models of the systems.

d^{-1} to search for δ Scuti- γ Doradus frequencies. A pre-whitening procedure was applied to extract all significant frequencies. The noise level was computed within a 2 d^{-1} window around each peak, and the signal-to-noise ratio (SNR) was defined as the ratio of the peak amplitude to this average noise amplitude. Only frequencies with an SNR of 5 or greater after pre-whitening were considered significant (Baran et al. 2015; Bowman & Michielsen 2021). All the significant frequencies were then simultaneously fitted using sinusoids in order to obtain their amplitudes and phases. We show the original periodogram for this curated data and after extraction of all the significant frequencies on Figure 6. A list of all the extracted frequencies, with their analytical errors (Montgomery & O'Donoghue 1999), for each of the system is provided in Appendix B.

8. Conclusions

In this study, we have presented a detailed analysis of five oEA systems selected from the CRÉME survey. By combining high-precision TESS photometry with multi-epoch high-resolution spectroscopy, we have derived precise LC and RV solutions that yield precise measurements of the orbital configuration of these binary systems and the fundamental stellar parameters.

MESA binary evolution simulations reveal that these systems have undergone either case A or case B mass transfer – a conclusion supported by the observed low mass ratios. These findings underscore the significant role that binary interactions and mass transfer play in shaping the evolutionary pathways of intermediate-mass stars.

However, we note that the adopted MESA-BINARY models for our systems do not fully reproduce the observed stellar properties. This discrepancy may arise from various factors, including the treatment of convective overshooting, mass transfer ef-

iciency, angular momentum loss, and stellar rotation. Further refinements are required to better align theoretical predictions with observations, which is crucial for accurately determining the progenitor properties and improving our understanding of the mass transfer process.

Our results contribute to the growing catalog of well-characterised oscillating EBs, providing essential benchmarks for testing and refining theoretical models of stellar structure and evolution. We aim to extend the asteroseismic analysis of these targets in a future study, specifically mode-identification using multi-colour photometry. Seismic modelling will help us further constrain the possible formation scenarios and provide insights on the changes in the internal structure and composition of the stars before and after the mass transfer process and the effect of such mass transfer events on the pulsation properties of the progenitors.

Acknowledgements

We acknowledge support provided by the Polish National Science Center through grants no. 2017/27/B/ST9/02727, 2021/41/N/ST9/02746, 2021/43/B/ST9/02972, 2023/49/B/ST9/01671, and 2024/53/N/ST9/03885. A. Moharana acknowledges support from the UK Science and Technology Facilities Council (STFC) under grant number ST/Y002563/1.

This research made use of data collected at ESO under programmes 088.D-0080, 089.D-0097, 090.D-0061, 091.D-0145, 094.A-9029, as well as through CNTAC proposal 2014B-067.

This research is based in part on data collected at Subaru Telescope, which is operated by the National Astronomical Observatory of Japan. We are honored and grateful for the oppor-

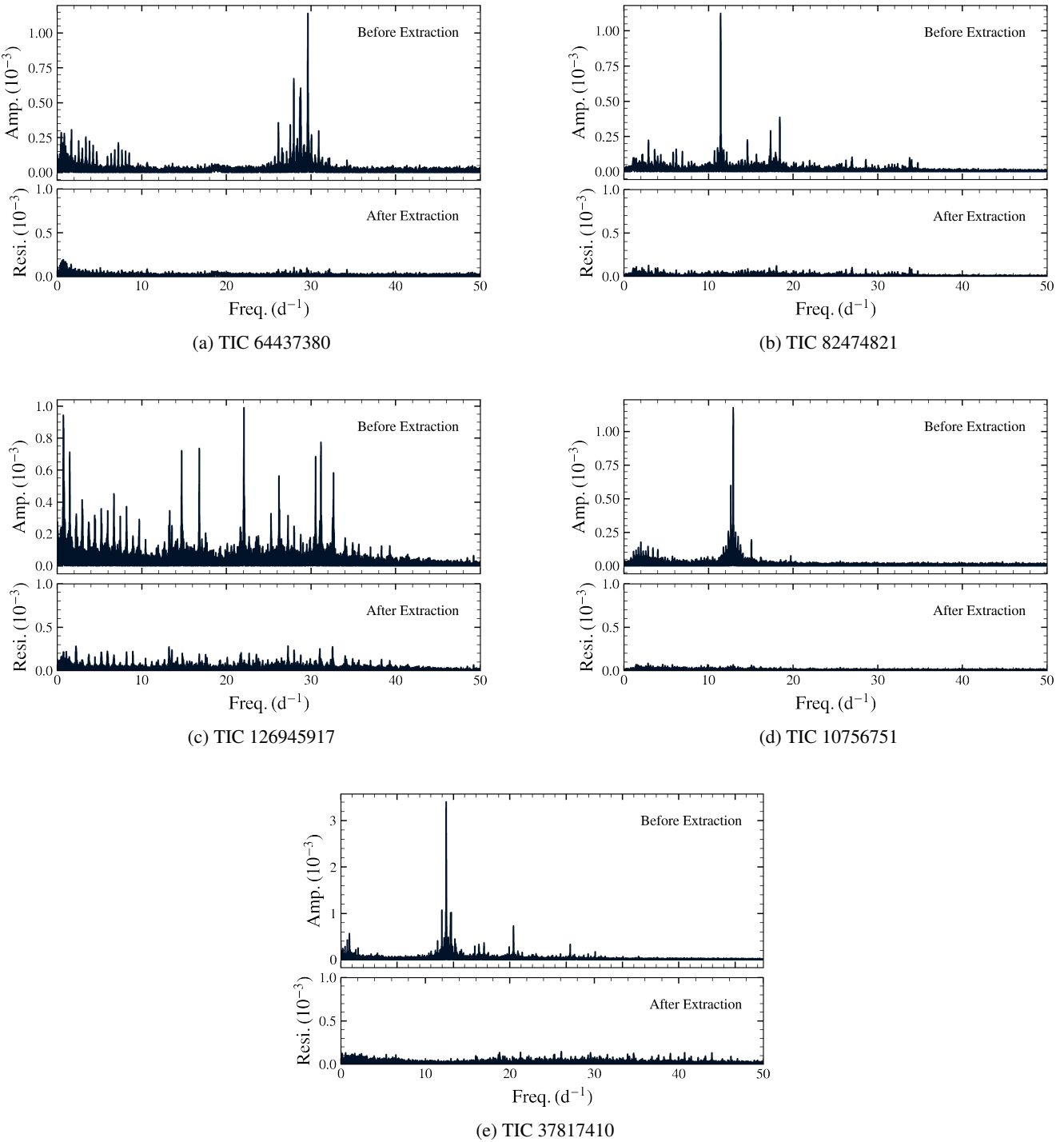


Fig. 6: Periodograms for residuals obtained after subtracting binary models from the corresponding LCs.

tunity of observing the Universe from Maunakea, which has the cultural, historical and natural significance in Hawaii.

This research made use of Lightkurve, a Python package for *Kepler* and TESS data analysis (Lightkurve Collaboration et al. 2018). This research uses data collected by the TESS mission (Guest Investigator proposals: G011083, G011154, G03028, G03251, G04047, G04171, G04234, G05003, G05078, G05125, G06057) which are publicly available from the MAST portal. Funding for the TESS mission is provided by NASA's Science Mission directorate.

References

- Antoci, V., Cunha, M. S., Bowman, D. M., et al. 2019, MNRAS, 490, 4040
- Asplund, M., Grevesse, N., Sauval, A. J., & Scott, P. 2009, ARA&A, 47, 481
- Baran, A. S., Koen, C., & Pokrzywka, B. 2015, MNRAS, 448, L16
- Blanco-Cuaresma, S. 2019, MNRAS, 486, 2075
- Blanco-Cuaresma, S., Soubiran, C., Heiter, U., & Jofré, P. 2014, A&A, 569, A111
- Blöcker, T. 1995, A&A, 297, 727
- Bowman, D. M. & Michielsen, M. 2021, A&A, 656, A158
- Brahm, R., Jordán, A., & Espinoza, N. 2017, PASP, 129, 034002
- Buchler, J. R. & Yueh, W. R. 1976, ApJ, 210, 440

- Cassisi, S., Potekhin, A. Y., Pietrinferni, A., Catelan, M., & Salaris, M. 2007, *ApJ*, 661, 1094
- Chen, X., Ding, X., Cheng, L., et al. 2022, *ApJS*, 263, 34
- Choi, J., Dotter, A., Conroy, C., et al. 2016, *ApJ*, 823, 102
- Chugunov, A. I., DeWitt, H. E., & Yakovlev, D. G. 2007, *Phys. Rev. D*, 76, 025028
- Claret, A. 2017, *A&A*, 600, A30
- Conroy, K. E., Kochoska, A., Hey, D., et al. 2020, *ApJS*, 250, 34
- Cyburt, R. H., Amthor, A. M., Ferguson, R., et al. 2010, *ApJS*, 189, 240
- Eggleton, P. 2006, Evolutionary Processes in Binary and Multiple Stars
- Eggleton, P. P. 1983a, *ApJ*, 268, 368
- Eggleton, P. P. 1983b, *ApJ*, 268, 368
- Ferguson, J. W., Alexander, D. R., Allard, F., et al. 2005, *ApJ*, 623, 585
- Foreman-Mackey, D., Hogg, D. W., Lang, D., & Goodman, J. 2013, *PASP*, 125, 306
- Fuller, G. M., Fowler, W. A., & Newman, M. J. 1985, *ApJ*, 293, 1
- Gaia Collaboration, Vallenari, A., Brown, A. G. A., et al. 2023, *A&A*, 674, A1
- Han, Z., Podsiadlowski, P., Maxted, P. F. L., & Marsh, T. R. 2003, *MNRAS*, 341, 669
- Han, Z., Podsiadlowski, P., Maxted, P. F. L., Marsh, T. R., & Ivanova, N. 2002, *MNRAS*, 336, 449
- Helminiak, K. G., Graczyk, D., Konacki, M., et al. 2015, *MNRAS*, 448, 1945
- Helminiak, K. G., Konacki, M., Różyczka, M., et al. 2012, *MNRAS*, 425, 1245
- Helminiak, K. G., Moharana, A., Pawar, T., et al. 2021, *MNRAS*, 508, 5687
- Helminiak, K. G., Tokovinin, A., Niemczura, E., et al. 2019, *A&A*, 622, A114
- Helminiak, K. G., Ukita, N., Kambe, E., et al. 2016, *MNRAS*, 461, 2896
- Henyey, L., Vardya, M. S., & Bodenheimer, P. 1965, *ApJ*, 142, 841
- Herwig, F. 2000, *A&A*, 360, 952
- Hippke, M., David, T. J., Mulders, G. D., & Heller, R. 2019, *AJ*, 158, 143
- Horvat, M., Conroy, K. E., Pablo, H., et al. 2018, *ApJS*, 237, 26
- Iglesias, C. A. & Rogers, F. J. 1993, *ApJ*, 412, 752
- Iglesias, C. A. & Rogers, F. J. 1996, *ApJ*, 464, 943
- Irwin, A. W. 2004, The FreeEOS Code for Calculating the Equation of State for Stellar Interiors
- Itoh, N., Hayashi, H., Nishikawa, A., & Kohyama, Y. 1996, *ApJS*, 102, 411
- Izumiura, H. 1999, in Observational Astrophysics in Asia and its Future, ed. P. S. Chen, Vol. 4, 77
- Jermyn, A. S., Bauer, E. B., Schwab, J., et al. 2023, *ApJS*, 265, 15
- Kahraman Aliçavuş, F., Çoban, Ç. G., Çelik, E., et al. 2023, *MNRAS*, 524, 619
- Kahraman Aliçavuş, F., Güümüş, D., Kırmızıtaş, Ö., et al. 2022a, Research in Astronomy and Astrophysics, 22, 085003
- Kahraman Aliçavuş, F., Handler, G., Aliçavuş, F., et al. 2022b, *MNRAS*, 510, 1413
- Kahraman Aliçavuş, F., Soydugan, E., Smalley, B., & Kubát, J. 2017, *MNRAS*, 470, 915
- Kaufer, A., Stahl, O., Tubbesing, S., et al. 1999, *The Messenger*, 95, 8
- Kippenhahn, R., Ruschenplatt, G., & Thomas, H. C. 1980, *A&A*, 91, 175
- Kippenhahn, R. & Weigert, A. 1967, *ZAp*, 65, 251
- Kobayashi, N., Tokunaga, A. T., Terada, H., et al. 2000, in Society of Photo-Optical Instrumentation Engineers (SPIE) Conference Series, Vol. 4008, Optical and IR Telescope Instrumentation and Detectors, ed. M. Iye & A. F. Moorwood, 1056–1066
- Koch, D. G., Borucki, W. J., Basri, G., et al. 2010, *ApJ*, 713, L79
- Kolb, U. & Ritter, H. 1990, *A&A*, 236, 385
- Konacki, M., Mutterspaugh, M. W., Kulkarni, S. R., & Helminiak, K. G. 2010, *ApJ*, 719, 1293
- Kurucz, R. L. 1979, *ApJS*, 40, 1
- Kurucz, R. L. 2005, Memorie della Societa Astronomica Italiana Supplementi, 8, 14
- Langanke, K. & Martínez-Pinedo, G. 2000, *Nuclear Physics A*, 673, 481
- Langer, N., El Eid, M. F., & Fricke, K. J. 1985, *A&A*, 145, 179
- Lenz, P. & Breger, M. 2005, Communications in Asteroseismology, 146, 53
- Liakos, A. 2024, arXiv e-prints, arXiv:2410.00763
- Liakos, A. & Niarchos, P. 2017, *MNRAS*, 465, 1181
- Liakos, A. & Niarchos, P. 2017a, *Monthly Notices of the Royal Astronomical Society*, 465, 1188
- Liakos, A. & Niarchos, P. 2017b, *Monthly Notices of the Royal Astronomical Society*, 465, 1214
- Liakos, A. & Niarchos, P. 2020, *Galaxies*, 8, 75
- Lightkurve Collaboration, Cardoso, J. V. d. M., Hedges, C., et al. 2018, Lightkurve: Kepler and TESS time series analysis in Python, *Astrophysics Source Code Library*
- Mahalanobis, P. 1936, On the generalised distance in statistics, 2, 49
- Marcadon, F. & Prša, A. 2024, *ApJ*, 976, 242
- Milone, E. E. 1968, *AJ*, 73, 708
- Miszuda, A., Kołaczek-Szymański, P. A., Szewczuk, W., & Daszyńska-Daszkiewicz, J. 2022, *MNRAS*, 514, 622
- Mkrtychian, D., Kusakin, A., Rodriguez, E., et al. 2004, *Astronomy & Astrophysics*, 419, 1015

Appendix A: Eclipse Minima Times

Appendix B: Pulsation Frequencies

Table A.1: Times of primary (integer cycle) and secondary (half-integer cycle) eclipse minima for the target TIC 64437380

BJD-2457000	Cycle	1- σ	BJD-2457000	Cycle	1- σ	BJD-2457000	Cycle	1- σ
2362.396193	-301.5	0.000364	2382.344695	-293.0	0.000090	3079.377001	4.0	0.000099
2363.569631	-301.0	0.000099	2383.519211	-292.5	0.000385	3080.550676	4.5	0.000328
2364.743176	-300.5	0.000342	2384.691686	-292.0	0.000096	3081.723891	5.0	0.000099
2365.916519	-300.0	0.000091	2385.866477	-291.5	0.000369	3082.897978	5.5	0.000405
2367.090087	-299.5	0.000302	2387.038335	-291.0	0.000095	3084.070877	6.0	0.000102
2368.263561	-299.0	0.000097	2388.212779	-290.5	0.000338	3085.244844	6.5	0.000358
2369.437316	-298.5	0.000343	2389.385625	-290.0	0.000101	3086.417780	7.0	0.000097
2370.610299	-298.0	0.000098	3068.814548	-0.5	0.000394	3087.592269	7.5	0.000366
2371.784380	-297.5	0.000345	3069.989692	0.0	0.000104	3088.764684	8.0	0.000100
2372.957192	-297.0	0.000093	3071.163243	0.5	0.000257	3089.938724	8.5	0.000367
2374.131110	-296.5	0.000283	3072.336533	1.0	0.000098	3091.111695	9.0	0.000098
2376.477589	-295.5	0.000369	3073.509847	1.5	0.000394	3092.286170	9.5	0.000403
2377.650928	-295.0	0.000089	3074.683356	2.0	0.000101	3093.458533	10.0	0.000099
2378.825263	-294.5	0.000266	3075.857370	2.5	0.000378	3094.632899	10.5	0.000370
2379.997904	-294.0	0.000090	3077.030191	3.0	0.000101	3095.805511	11.0	0.000107
2381.171891	-293.5	0.000322	3078.203905	3.5	0.000371			

Table A.2: Times of primary (integer cycle) and secondary (half-integer cycle) eclipse minima for the target TIC 82474821

BJD-2457000	Cycle	1- σ	BJD-2457000	Cycle	1- σ	BJD-2457000	Cycle	1- σ
2229.519557	-277.0	0.000071	2266.613007	-263.5	0.003327	2983.668094	-2.5	0.000431
2230.897484	-276.5	0.000353	2268.507459	-263.0	0.182495	2985.037314	-2.0	0.000064
2232.266973	-276.0	0.000072	2269.362539	-262.5	0.003154	2986.415628	-1.5	0.000320
2233.644984	-275.5	0.000341	2270.729715	-262.0	0.000742	2987.784656	-1.0	0.000070
2235.014119	-275.0	0.000073	2272.094526	-261.5	0.002129	2989.162642	-0.5	0.000312
2236.392158	-274.5	0.000329	2273.477106	-261.0	0.000846	2990.532038	0.0	0.000073
2237.761462	-274.0	0.000077	2274.849345	-260.5	0.002542	2991.909698	0.5	0.000360
2239.138815	-273.5	0.000518	2276.224417	-260.0	0.000761	2993.279487	1.0	0.000067
2240.508938	-273.0	0.000072	2277.598701	-259.5	0.001996	2994.656550	1.5	0.000330
2243.256098	-272.0	0.000076	2278.971788	-259.0	0.000731	2996.026867	2.0	0.000068
2244.633544	-271.5	0.000351	2963.058400	-10.0	0.000092	2997.403772	2.5	0.000353
2246.003488	-271.0	0.000070	2964.437221	-9.5	0.000383	2998.774203	3.0	0.000065
2247.380696	-270.5	0.000807	2965.805988	-9.0	0.000072	3000.150676	3.5	0.000312
2248.750723	-270.0	0.000071	2967.184534	-8.5	0.000256	3001.521649	4.0	0.000069
2250.128238	-269.5	0.000411	2968.553322	-8.0	0.000072	3002.898341	4.5	0.000425
2251.498224	-269.0	0.000078	2969.931891	-7.5	0.000428	3004.268991	5.0	0.000067
2252.875028	-268.5	0.000462	2971.300504	-7.0	0.000068	3005.645087	5.5	0.000411
2255.622050	-267.5	0.001273	2972.679335	-6.5	0.000349	3007.016419	6.0	0.000069
2256.993027	-267.0	0.000583	2974.048015	-6.0	0.000067	3008.391846	6.5	0.000379
2258.369864	-266.5	0.002765	2975.425040	-5.5	0.000607	3009.763798	7.0	0.000066
2259.740416	-266.0	0.000649	2976.795260	-5.0	0.000078	3011.138809	7.5	0.000578
2261.115217	-265.5	0.003119	2978.173736	-4.5	0.000303	3012.511181	8.0	0.000067
2262.487751	-265.0	0.000754	2979.542649	-4.0	0.000069	3013.885406	8.5	0.000427
2263.864059	-264.5	0.003889	2980.920741	-3.5	0.000495			
2265.235091	-264.0	0.000622	2982.289848	-3.0	0.000102			

Table A.3: Times of primary (integer cycle) and secondary (half-integer cycle) eclipse minima for the target TIC 126945917

BJD–2457000	Cycle	$1-\sigma$	BJD–2457000	Cycle	$1-\sigma$	BJD–2457000	Cycle	$1-\sigma$
1325.624401	-530.5	0.000451	2039.745243	2.0	0.000095	2075.283022	28.5	0.000238
1326.291243	-530.0	0.000103	2040.416943	2.5	0.000296	2075.954571	29.0	0.000094
1326.965744	-529.5	0.000288	2041.086262	3.0	0.000093	2076.623998	29.5	0.000359
1327.632305	-529.0	0.000084	2041.758065	3.5	0.000317	2077.295631	30.0	0.000107
1328.306375	-528.5	0.000336	2042.427350	4.0	0.000092	2077.965481	30.5	0.000275
1328.973460	-528.0	0.000088	2043.099297	4.5	0.000317	2078.636687	31.0	0.000083
1329.647835	-527.5	0.000329	2043.768235	5.0	0.000095	2079.306818	31.5	0.000309
1330.314408	-527.0	0.000093	2044.440086	5.5	0.000364	2079.977753	32.0	0.000086
1330.988217	-526.5	0.000329	2045.109516	6.0	0.000085	2080.648042	32.5	0.000336
1331.655613	-526.0	0.000091	2045.781201	6.5	0.000346	2081.318806	33.0	0.000080
1332.329617	-525.5	0.000285	2046.450564	7.0	0.000093	2081.988969	33.5	0.000248
1332.996506	-525.0	0.000084	2047.121998	7.5	0.000274	2082.659827	34.0	0.000091
1333.670803	-524.5	0.000277	2047.791704	8.0	0.000096	2083.330184	34.5	0.000271
1334.337687	-524.0	0.000091	2049.132789	9.0	0.000119	2084.000925	35.0	0.000083
1335.012311	-523.5	0.000327	2049.804327	9.5	0.000232	3154.853333	833.5	0.000375
1335.678640	-523.0	0.000094	2050.473989	10.0	0.000096	3155.521829	834.0	0.000090
1336.352980	-522.5	0.000457	2051.145023	10.5	0.000315	3156.194623	834.5	0.000294
1337.019604	-522.0	0.000088	2051.814959	11.0	0.000081	3156.862943	835.0	0.000085
1337.693816	-521.5	0.000291	2052.486221	11.5	0.000254	3157.535633	835.5	0.000269
1338.360713	-521.0	0.000094	2053.156252	12.0	0.000097	3158.203988	836.0	0.000089
1339.701580	-520.0	0.000114	2053.826849	12.5	0.000339	3158.876918	836.5	0.000232
1340.375732	-519.5	0.000197	2054.497252	13.0	0.000097	3159.545041	837.0	0.000087
1341.042948	-519.0	0.000095	2055.168208	13.5	0.000296	3160.218065	837.5	0.000296
1341.717207	-518.5	0.000240	2055.838296	14.0	0.000092	3160.886119	838.0	0.000088
1342.383888	-518.0	0.000086	2056.508738	14.5	0.000427	3161.558909	838.5	0.000253
1343.057811	-517.5	0.000385	2057.179431	15.0	0.000098	3162.227088	839.0	0.000096
1343.724960	-517.0	0.000094	2057.850175	15.5	0.000258	3162.900133	839.5	0.000333
1344.399294	-516.5	0.000442	2058.520485	16.0	0.000089	3163.568231	840.0	0.000092
1345.066070	-516.0	0.000086	2059.190904	16.5	0.000329	3164.241169	840.5	0.000348
1345.740220	-515.5	0.000340	2059.861664	17.0	0.000085	3164.909259	841.0	0.000093
1346.407152	-515.0	0.000098	2060.531989	17.5	0.000230	3168.932336	844.0	0.000084
1347.081189	-514.5	0.000337	2061.870880	18.5	0.000446	3169.605456	844.5	0.000303
1347.748468	-514.0	0.000092	2062.543737	19.0	0.000095	3170.273441	845.0	0.000088
1348.422002	-513.5	0.001262	2063.213993	19.5	0.000363	3170.946689	845.5	0.000363
1349.089074	-513.0	0.000235	2063.884917	20.0	0.000084	3171.614611	846.0	0.000090
1349.763999	-512.5	0.000255	2064.554848	20.5	0.000297	3172.287721	846.5	0.000346
1350.430374	-512.0	0.000084	2065.226050	21.0	0.000088	3172.955643	847.0	0.000088
1351.104822	-511.5	0.000341	2065.896113	21.5	0.000247	3173.628501	847.5	0.000242
1351.771507	-511.0	0.000091	2066.567021	22.0	0.000084	3174.296724	848.0	0.000087
1352.445971	-510.5	0.000256	2067.236661	22.5	0.000252	3174.969441	848.5	0.000252
1353.112493	-510.0	0.000133	2067.908112	23.0	0.000094	3175.637867	849.0	0.000094
2036.394339	-0.5	0.000242	2068.577663	23.5	0.000203	3176.310933	849.5	0.000257
2037.063025	0.0	0.000091	2069.249207	24.0	0.000089	3176.978922	850.0	0.000093
2037.735419	0.5	0.000292	2069.918770	24.5	0.000408	3177.652184	850.5	0.000276
2038.404083	1.0	0.000092	2070.590238	25.0	0.000087	3178.319982	851.0	0.000089
2039.076336	1.5	0.000310	2071.259535	25.5	0.000419	3178.993127	851.5	0.000274

Table A.4: Times of primary (integer cycle) and secondary (half-integer cycle) eclipse minima for the target TIC 10756751

BJD–2457000	Cycle	$1-\sigma$	BJD–2457000	Cycle	$1-\sigma$	BJD–2457000	Cycle	$1-\sigma$
1386.258438	-522.5	0.000554	2462.440775	-214.0	0.000107	2495.584159	-204.5	0.000524
1387.997561	-522.0	0.000109	2464.188013	-213.5	0.000459	2497.325205	-204.0	0.000108
1389.747137	-521.5	0.000491	2465.929209	-213.0	0.000108	3208.967778	0.0	0.000112
1391.485993	-521.0	0.000101	2467.677443	-212.5	0.000429	3210.711594	0.5	0.000502
1393.235962	-520.5	0.000559	2469.417663	-212.0	0.000110	3212.455909	1.0	0.000100
1396.723826	-519.5	0.000647	2474.653491	-210.5	0.000495	3214.201061	1.5	0.000523
1398.463186	-519.0	0.000107	2476.394541	-210.0	0.000103	3215.944313	2.0	0.000107
1400.212003	-518.5	0.000599	2478.142102	-209.5	0.000430	3217.689992	2.5	0.000603
1401.951742	-518.0	0.000106	2479.882923	-209.0	0.000112	3222.921333	4.0	0.000101
1403.701315	-517.5	0.000474	2481.629650	-208.5	0.000412	3224.667606	4.5	0.000454
1405.440133	-517.0	0.000106	2488.605930	-206.5	0.000516	3226.409815	5.0	0.000115
2448.486848	-218.0	0.000103	2490.348526	-206.0	0.000105	3228.155380	5.5	0.000562
2450.234401	-217.5	0.000542	2492.095454	-205.5	0.000583	3229.898167	6.0	0.000115
2451.975367	-217.0	0.000104	2493.836936	-205.0	0.000113	3231.644278	6.5	0.000484

Table A.5: Times of primary (integer cycle) and secondary (half-integer cycle) eclipse minima for the target TIC 37817410

BJD–2457000	Cycle	1- σ	BJD–2457000	Cycle	1- σ	BJD–2457000	Cycle	1- σ
1438.007277	-0.5	0.001944	1457.552194	7.0	0.000072	2184.662999	286.0	0.000071
1439.309131	0.0	0.000070	1458.855020	7.5	0.000242	2185.979140	286.5	0.000565
1440.612396	0.5	0.001107	1460.158395	8.0	0.000070	2187.269224	287.0	0.000072
1441.915237	1.0	0.000075	1461.461928	8.5	0.000564	2188.574951	287.5	0.000442
1443.220008	1.5	0.000409	1462.764513	9.0	0.000078	2189.875199	288.0	0.000065
1444.521329	2.0	0.000078	1464.067669	9.5	0.000549	2191.180115	288.5	0.000943
1445.825641	2.5	0.000599	2174.238577	282.0	0.000090	2192.481387	289.0	0.000073
1447.127503	3.0	0.000075	2175.544447	282.5	0.000361	2193.786243	289.5	0.000551
1448.431964	3.5	0.000809	2176.844705	283.0	0.000073	2195.087532	290.0	0.000073
1449.733627	4.0	0.000079	2178.150458	283.5	0.000652	2196.392149	290.5	0.000914
1452.339858	5.0	0.000075	2179.450782	284.0	0.000077	2197.693696	291.0	0.000072
1453.642769	5.5	0.000477	2180.756363	284.5	0.000566	2198.997590	291.5	0.000702
1454.946031	6.0	0.000071	2182.056855	285.0	0.000069	2200.299252	292.0	0.000139
1456.249326	6.5	0.000566	2183.362848	285.5	0.000321			

Table B.1: Frequencies used to compute the Least-Squares Fourier fitting for the target TIC 64437380

Label	Frequency (d ⁻¹)	Amplitude	Phase
F1	29.631632 ± 9.28e-06	0.000997 ± 1.24e-05	0.700701 ± 0.001965
F2	27.973431 ± 1.30e-05	0.000712 ± 1.24e-05	0.039448 ± 0.002769
F3	28.688072 ± 1.82e-05	0.000468 ± 1.24e-05	0.970814 ± 0.003872
F4	28.776626 ± 2.54e-05	0.000360 ± 1.24e-05	0.090007 ± 0.005397
F5	26.149574 ± 2.67e-05	0.000348 ± 1.24e-05	0.105014 ± 0.005657
F6	1.7057163 ± 3.28e-05	0.000282 ± 1.24e-05	0.119956 ± 0.006951
F7	0.4896069 ± 2.92e-05	0.000317 ± 1.24e-05	0.243341 ± 0.006188
F8	29.662922 ± 3.17e-05	0.000291 ± 1.24e-05	0.661731 ± 0.006718
F9	27.124015 ± 3.34e-05	0.000276 ± 1.24e-05	0.687824 ± 0.007091
F10	3.4059107 ± 2.74e-05	0.000338 ± 1.24e-05	0.237469 ± 0.005810
F11	4.2595528 ± 3.77e-05	0.000246 ± 1.24e-05	0.554921 ± 0.007999
F12	2.5537002 ± 3.44e-05	0.000271 ± 1.24e-05	0.528809 ± 0.007298
F13	0.8575960 ± 3.94e-05	0.000236 ± 1.24e-05	0.499437 ± 0.008357
F14	7.2421192 ± 3.42e-05	0.000272 ± 1.24e-05	0.034559 ± 0.007251
F15	0.6084296 ± 4.48e-05	0.000206 ± 1.24e-05	0.852651 ± 0.009492
F16	30.917208 ± 4.65e-05	0.000163 ± 1.24e-05	0.427604 ± 0.009849
F17	8.0957614 ± 4.48e-05	0.000207 ± 1.24e-05	0.350799 ± 0.009497
F18	6.3913841 ± 5.47e-05	0.000170 ± 1.24e-05	0.746607 ± 0.011592
F19	29.706199 ± 5.23e-05	0.000137 ± 1.24e-05	0.578408 ± 0.011089
F20	29.557108 ± 6.48e-05	0.000129 ± 1.24e-05	0.798661 ± 0.013720
F21	30.916514 ± 4.54e-05	0.000129 ± 1.24e-05	0.556667 ± 0.009624
F22	28.690173 ± 2.36e-05	0.000129 ± 1.24e-05	0.528247 ± 0.005002

Table B.2: Frequencies used to compute the Least-Squares Fourier fitting for the target TIC 82474821

Label	Frequency (d ⁻¹)	Amplitude	Phase
F1	11.438400 ± 4.33e-06	0.001147 ± 6.95e-06	0.138650 ± 0.000948
F2	18.428984 ± 1.28e-05	0.000393 ± 6.95e-06	0.312123 ± 0.002815
F3	17.336435 ± 1.72e-05	0.000293 ± 6.95e-06	0.402974 ± 0.003775
F4	2.9103399 ± 2.57e-05	0.000196 ± 6.95e-06	0.909752 ± 0.005629
F5	14.600872 ± 2.29e-05	0.000220 ± 6.95e-06	0.302139 ± 0.005028
F6	6.1912872 ± 3.80e-05	0.000132 ± 6.95e-06	0.503004 ± 0.008320
F7	17.927163 ± 3.40e-05	0.000148 ± 6.95e-06	0.184552 ± 0.007456
F8	3.6437002 ± 2.43e-05	0.000186 ± 6.95e-06	0.365693 ± 0.005334
F9	3.6416541 ± 2.63e-05	0.000171 ± 6.95e-06	0.452262 ± 0.005751
F10	4.3695361 ± 3.45e-05	0.000145 ± 6.95e-06	0.722033 ± 0.007552
F11	11.434968 ± 3.05e-05	0.000142 ± 6.95e-06	0.250010 ± 0.006684
F12	6.9172551 ± 3.66e-05	0.000134 ± 6.95e-06	0.044063 ± 0.008006
F13	5.8248381 ± 2.87e-05	0.000155 ± 6.95e-06	0.795300 ± 0.006280
F14	5.8186998 ± 2.93e-05	0.000149 ± 6.95e-06	0.047370 ± 0.006408
F15	15.666161 ± 3.99e-05	0.000126 ± 6.95e-06	0.034572 ± 0.008745

Table B.3: Frequencies used to compute the Least-Squares Fourier fitting for the target TIC 126945917

Label	Frequency (d^{-1})	Amplitude	Phase
F1	22.073819 \pm 3.56e-06	0.000993 \pm 1.18e-05	0.107520 \pm 0.001889
F2	0.7297407 \pm 3.34e-06	0.001045 \pm 1.18e-05	0.380749 \pm 0.001771
F3	0.7737380 \pm 4.43e-06	0.000776 \pm 1.18e-05	0.909715 \pm 0.002353
F4	31.171173 \pm 4.82e-06	0.000731 \pm 1.18e-05	0.326682 \pm 0.002557
F5	16.794981 \pm 4.78e-06	0.000740 \pm 1.18e-05	0.472750 \pm 0.002536
F6	1.4907642 \pm 4.02e-06	0.000864 \pm 1.18e-05	0.217327 \pm 0.002135
F7	14.714690 \pm 4.87e-06	0.000726 \pm 1.18e-05	0.589102 \pm 0.002584
F8	30.541814 \pm 4.56e-06	0.000771 \pm 1.18e-05	0.511148 \pm 0.002417
F9	26.217196 \pm 6.25e-06	0.000567 \pm 1.18e-05	0.966106 \pm 0.003314
F10	32.659786 \pm 6.65e-06	0.000532 \pm 1.18e-05	0.491052 \pm 0.003526
F11	6.7095688 \pm 6.16e-06	0.000569 \pm 1.18e-05	0.957445 \pm 0.003267
F12	30.545354 \pm 7.98e-06	0.000438 \pm 1.18e-05	0.789437 \pm 0.004231
F13	8.2021572 \pm 7.77e-06	0.000449 \pm 1.18e-05	0.364410 \pm 0.004123
F14	5.2192946 \pm 7.81e-06	0.000447 \pm 1.18e-05	0.624241 \pm 0.004143
F15	2.9529954 \pm 8.31e-06	0.000428 \pm 1.18e-05	0.661682 \pm 0.004405
F16	0.7011805 \pm 8.17e-06	0.000415 \pm 1.18e-05	0.105064 \pm 0.004331
F17	5.9735661 \pm 7.23e-06	0.000486 \pm 1.18e-05	0.450736 \pm 0.003833
F18	7.4621794 \pm 8.77e-06	0.000400 \pm 1.18e-05	0.133543 \pm 0.004649
F19	4.4964966 \pm 8.12e-06	0.000424 \pm 1.18e-05	0.281985 \pm 0.004308
F20	3.0124028 \pm 8.57e-06	0.000405 \pm 1.18e-05	0.520629 \pm 0.004543
F21	1.5297247 \pm 1.05e-05	0.000319 \pm 1.18e-05	0.598491 \pm 0.005582
F22	4.4486331 \pm 1.01e-05	0.000347 \pm 1.18e-05	0.970609 \pm 0.005372
F23	25.274629 \pm 1.03e-05	0.000342 \pm 1.18e-05	0.767988 \pm 0.005467
F24	13.294523 \pm 1.02e-05	0.000346 \pm 1.18e-05	0.027543 \pm 0.005417
F25	26.278536 \pm 1.10e-05	0.000319 \pm 1.18e-05	0.703953 \pm 0.005850
F26	9.6994829 \pm 1.06e-05	0.000329 \pm 1.18e-05	0.239402 \pm 0.005659
F27	0.8187155 \pm 1.08e-05	0.000344 \pm 1.18e-05	0.300980 \pm 0.005729
F28	1.4616867 \pm 1.02e-05	0.000344 \pm 1.18e-05	0.577823 \pm 0.005417
F29	3.7196275 \pm 1.16e-05	0.000297 \pm 1.18e-05	0.636138 \pm 0.006194
F30	27.277788 \pm 1.24e-05	0.000284 \pm 1.18e-05	0.744833 \pm 0.006588

Table B.4: Frequencies used to compute the Least-Squares Fourier fitting for the target TIC 10756751

Label	Frequency (d^{-1})	Amplitude	Phase
F1	12.920924 \pm 1.65e-06	0.001171 \pm 6.49e-06	0.499714 \pm 0.0008
F2	12.639542 \pm 2.74e-06	0.000706 \pm 6.49e-06	0.481234 \pm 0.0014
F3	12.924281 \pm 7.03e-06	0.0000250 \pm 6.49e-06	0.882769 \pm 0.0037
F4	2.0107661 \pm 8.07e-06	0.0000221 \pm 6.49e-06	0.668651 \pm 0.0043
F5	15.074520 \pm 1.11e-05	0.0000172 \pm 6.49e-06	0.450698 \pm 0.0059
F6	2.8653349 \pm 7.00e-06	0.0000264 \pm 6.49e-06	0.460549 \pm 0.0037
F7	2.2893068 \pm 7.81e-06	0.0000232 \pm 6.49e-06	0.857032 \pm 0.0041
F8	1.7169598 \pm 8.97e-06	0.0000191 \pm 6.49e-06	0.208902 \pm 0.0047
F9	3.4386022 \pm 1.00e-05	0.0000194 \pm 6.49e-06	0.886262 \pm 0.0053
F10	2.5840063 \pm 1.15e-05	0.0000160 \pm 6.49e-06	0.083443 \pm 0.0061
F11	4.0173640 \pm 1.35e-05	0.0000146 \pm 6.49e-06	0.642853 \pm 0.0072
F12	12.408042 \pm 1.53e-05	0.0000122 \pm 6.49e-06	0.534624 \pm 0.0081
F13	1.7189086 \pm 1.25e-05	0.0000128 \pm 6.49e-06	0.409329 \pm 0.0066
F14	2.2939623 \pm 1.44e-05	0.0000113 \pm 6.49e-06	0.364557 \pm 0.0077
F15	2.0142847 \pm 1.95e-05	0.0000009 \pm 6.49e-06	0.880057 \pm 0.0104
F16	19.719587 \pm 2.47e-05	0.0000007 \pm 6.49e-06	0.663119 \pm 0.0132

Table B.5: Frequencies used to compute the Least-Squares Fourier fitting for the target TIC 37817410

Label	Frequency (d^{-1})	Amplitude	Phase
F1	$18.718979 \pm 1.50\text{e-}06$	$0.003378 \pm 1.17\text{e-}05$	0.880115 ± 0.000554
F2	$19.611191 \pm 4.44\text{e-}06$	$0.001059 \pm 1.08\text{e-}05$	0.934496 ± 0.001634
F3	$30.664819 \pm 6.36\text{e-}06$	$0.000737 \pm 1.08\text{e-}05$	0.146838 ± 0.002340
F4	$1.5341865 \pm 7.70\text{e-}06$	$0.000685 \pm 1.15\text{e-}05$	0.600564 ± 0.002855
F5	$1.1545303 \pm 8.75\text{e-}06$	$0.000583 \pm 1.14\text{e-}05$	0.029044 ± 0.003227
F6	$25.429543 \pm 1.17\text{e-}05$	$0.000397 \pm 1.08\text{e-}05$	0.316141 ± 0.004338
F7	$40.727537 \pm 1.39\text{e-}05$	$0.000336 \pm 1.08\text{e-}05$	0.334563 ± 0.005116
F8	$24.520260 \pm 1.45\text{e-}05$	$0.000320 \pm 1.08\text{e-}05$	0.318793 ± 0.005365
F9	$1.9097716 \pm 1.41\text{e-}05$	$0.000358 \pm 1.14\text{e-}05$	0.093028 ± 0.005247
F10	$24.557621 \pm 1.99\text{e-}05$	$0.000244 \pm 1.13\text{e-}05$	0.974350 ± 0.007436
F11	$20.451530 \pm 1.74\text{e-}05$	$0.000268 \pm 1.08\text{e-}05$	0.441621 ± 0.006415
F12	$18.981561 \pm 1.68\text{e-}05$	$0.000280 \pm 1.09\text{e-}05$	0.799792 ± 0.006189
F13	$0.3416380 \pm 1.86\text{e-}05$	$0.000273 \pm 1.12\text{e-}05$	0.597371 ± 0.006818
F14	$2.3015752 \pm 2.26\text{e-}05$	$0.000223 \pm 1.16\text{e-}05$	0.080970 ± 0.008362
F15	$23.791677 \pm 2.34\text{e-}05$	$0.000207 \pm 1.13\text{e-}05$	0.751740 ± 0.008717
F16	$19.575011 \pm 2.41\text{e-}05$	$0.000196 \pm 1.08\text{e-}05$	0.266198 ± 0.008892
F17	$18.422385 \pm 2.44\text{e-}05$	$0.000198 \pm 1.09\text{e-}05$	0.329637 ± 0.008963
F18	$0.2565404 \pm 2.44\text{e-}05$	$0.000191 \pm 1.10\text{e-}05$	0.611227 ± 0.008964
F19	$18.693240 \pm 2.44\text{e-}05$	$0.000210 \pm 1.17\text{e-}05$	0.199131 ± 0.008976
F20	$0.4231242 \pm 2.68\text{e-}05$	$0.000186 \pm 1.13\text{e-}05$	0.163392 ± 0.009849
F21	$45.158968 \pm 2.88\text{e-}05$	$0.000162 \pm 1.08\text{e-}05$	0.854718 ± 0.010601